Supplementary Information

Fine-regulating of gradient gate-opening in nanoporous crystals for sieving separation of ternary C3 hydrocarbons

Shuang Liu,[a,+] Yuhang Huang,[b,+] Jingmeng Wan,[b] Jia-jia Zheng,[c] Rajamani Krishna,[d] Yi Li,[b] Kai Ge,[b,*] Jie Tang,[b] Jingui Duan[b,*]

[a] Henan Engineering Research Centre for Green Synthesis of Pharmaceuticals, College of Chemistry and Chemical Engineering, Shangqiu Normal University, Shangqiu, 476000, China.

[b] State Key Laboratory of Materials-Oriented Chemical Engineering, College of Chemical Engineering, Nanjing Tech University, Nanjing, 211816, China.

[c] Laboratory of Theoretical and Computational Nanoscience, CAS Center for Excellence in Nanoscience, National Center for Nanoscience and Technology, Chinese Academy of Sciences, Beijing 100190, China.

[d] Van 't Hoff Institute for Molecular Sciences, University of Amsterdam, Science Park 904, 1098 XH Amsterdam, The Netherlands.

Email: gekai@njtech.edu.cn (K. G.); duanjingui@njtech.edu.cn (J. D.)

General Procedures and Materials

All reagents and solvents were commercially available and used as received. The Fourier-transform Infrared (FT-IR) spectra were recorded from KBr pellets in the range of 4000–600 cm^{-1} on a VECTOR 22 spectrometer. Thermogravimetric analyses (TGA) were performed using a STA 209 F1 (NETZSCH Instruments) thermo-microbalance, heating from room temperature to 650°C at a rate of 10°C min^{-1} under nitrogen flow. Simulated powder patterns from single-crystal X-ray diffraction data were generated using Mercury 1.4.2 software. The coincident PXRD/adsorption measurements were performed with a Rigaku SmartLab with CuKα radiation connected to a BELSORP-18PLUS volumetric adsorption setup (MicrotracBEL Japan, Inc.) equipped with a custom-made cryostat apparatus. The respective apparatuses were synchronized to enable each PXRD pattern to be obtained at each equilibrium point of the sorption isotherms.

Synthesis of NTU-65-series. A solution of **L** (0.50 mmol) in *N*, *N'*-dimethylformamide (DMF) (1 mL) was slowly layered on aqueous solution (0.5 mL) of $M1(BF_6)_2{\cdot}6H_2O$ (0.014 mmol, M1: Fe^{2+}, Co^{2+}) and $(NH_4)_2M2F_6{\cdot}6H_2O$ (0.014 mmol, M2: Zr^{4+}, Ti^{4+}). After a week, single-crystals of NTU-65 derivates (named as **NTU-65-FeZr**, **NTU-65-FeTi**, **NTU-65-CoZr** and **NTU-65-CoTi**, respectively) were obtained. Yield: ~40-60%, based on **L**.

Single crystal X-ray studies. Single-crystal X-ray diffraction measurements were performed on a Bruker Smart Apex CCD diffractometer at 298 K using graphite monochromator Mo/Kα radiation (λ = 0.71073 Å). Data reduction was made with the Bruker Saint program. The structures were solved by direct methods and refined with full-matrix least squares technique using the SHELXTL package[1]. Non-hydrogen atoms were refined with anisotropic displacement parameters during the final cycles. Organic hydrogen atoms were placed in calculated positions with isotropic displacement parameters set to 1.2 × Ueq of the attached atom. The unit cell includes disordered solvent molecules, which could not be modeled as discrete atomic sites. We employed PLATON/SQUEEZE[2, 3] to calculate the diffraction contribution of the solvent molecules and, thereby, to produce a set of solvent-free diffraction intensities; structures were then refined again using the data generated. Crystal data are summarized in Table S1.

Activation of NTU-65-series. Solvent-exchanged crystal was prepared by immersing the as-synthesized samples in dry MeOH for two days to remove the nonvolatile solvents, and the extract

was decanted every 8 h and fresh acetone was replaced. The completely activated sample was obtained by heating the solvent-exchanged sample at 25°C for 6 h, 60°C for 6 h and then 120°C for 20 h under a dynamic high vacuum.

Single-gas sorption measurements. Gas adsorptions were performed on a Belsorp volumetric adsorption instrument (BEL Japan Corp.). In the sorption measurements, ultra-high-purity grade gases were used throughout the experiments.

In-situ X-ray study. The fully activated crystals that loaded inside a double-layer sealed beryllium ball were purged by C_3H_4 at 273 K, respectively. The X-ray diffractions were then collected at different pressures according to the corresponding isotherms. The system pressure was regulated by a controller that contains an automatic dosing system and pressure sensor (0.01-100 kPa). For each measurement, PXRD was collected at 20 min later, after adsorption reaches equilibrium at this pressure.

Fitting of unary isotherm data. The unary isotherm data for C_3H_4, C_3H_6 and C_3H_8, measured at three different temperatures 273 K, 283 K, and 298 K in **NTU-65-FeZr**, **NTU-65-FeTi**, **NTU-65-CoZr** and **NTU-65-CoTi** were fitted with good accuracy using the dual-site Langmuir-Freundlich model, where we distinguish two distinct adsorption sites A and B:

$$q = \frac{q_{sat,A} b_A p^{\nu A}}{1 + b_A p^{\nu A}} + \frac{q_{sat,B} b_B p^{\nu B}}{1 + b_B p^{\nu B}} \tag{S1}$$

In eq (S1), the Langmuir-Freundlich parameters b_A, b_B are both temperature dependent

$$b_A = b_{A0} \exp\left(\frac{E_A}{RT}\right); \quad b_b = b_{B0} \exp\left(\frac{E_B}{RT}\right) \tag{S2}$$

In eq (S2), E_A, E_B are the energy parameters associated with sites A, and B, respectively.

The fit parameters are provided in Table S4-S7,

Isosteric heat of adsorption. The isosteric heat of adsorption, Q_{st}, is defined as

$$Q_{st} = -RT^2 \left(\frac{\partial \ln p}{\partial T}\right)_q \tag{S3}$$

where the derivative in the right member of eq (S3) is determined at constant adsorbate loading, q. The derivative was determined by analytic differentiation of the combination of eq (S1), eq (S2), and eq (S3).

IAST selectivities. The IAST was used to determine the selectivities for binary 50/50 C_3H_6/C_3H_8 and 1/99 C_3H_4/C_3H_6 mixtures at 273 K, 283 K, and 298 K.

Transient breakthrough simulations. Transient breakthrough experiments were carried out for binary 50/50 C_3H_6/C_3H_8 and 1/99 C_3H_4/C_3H_6 mixtures at a total pressure of 100 kPa and 273 K. The sample mass of MOF in the packed bed, m_{ads} is 1 g. The flow rates at the inlet, Q_0 = 5 mL min^{-1}. Transient breakthrough simulations were carried out using the methodology described in earlier publications.[4-8] In these simulations, intra-crystalline diffusion influences are ignored.

Breakthrough measurements. All experiments were performed on a breakthrough instrument (CT-4, Xuzhou North Gaorui). The initial activated series crystals were tightly packed into a stainless-steel column (ϕ = 0.5 cm, *L* = 16.0 cm). Then, the column was activated under vacuum at corresponding temperature and then swept with He flow to remove impurities. Until no any signal was detected, the gas flow was dosed into the column. Breakpoints were determined by gas chromatography. Between cycling experiments, regeneration can be achieved under vacuum at 393 K for 2 h.

Computational Details. Adsorption energies for C_3H_4 were calculated to understand the order in softness of **NTU-65-series**. We carried out canonical Monte-Carlo (MC) simulation[9] to locate C_3H_4 positions in these PCPs, as implemented in RASPA.[10] The Lennard-Jones (LJ) potentials were used to describe the Van der Waals interaction of gas molecules with PCP framework and the electrostatic interaction was evaluated with the Ewald summation method. The LJ parameters for PCP framework were taken from the standard universal force field (UFF)[11] and the DDEC atomic charges[12] of PCP framework were used in the evaluation of electrostatic interaction. The LJ parameters and atomic charges of C_3H_4 were taken from literature.[13] In the MC simulation, the first 1×10^5 cycles were employed for obtaining equilibration and then 3×10^5 cycles were used for obtaining distribution of guest molecule. The final gas adsorption configuration obtained by above MC simulation was used

to construct the initial structure for performing geometry optimization with density functional theory (DFT).

The Perdew-Burke-Ernzerhof functional[14] with Grimme's semi-empirical "D3" dispersion term[15] (PBE-D3), as implemented in the Vienna Ab initio Simulation Package (VASP 5.4.1),[16, 17] was employed in these calculations. The plane wave basis sets with an energy cutoff of 500 eV were used to describe valence electrons and the projector-augmented-wave pseudopotentials[18, 19] were used to describe core electrons. The criterion of atomic force for geometry optimization was set to be 0.02 eV/Å. The Brillouin zone was sampled by a Γ-point in these calculations. Hubbard *U* corrections[20] were applied to the *d* electrons of Ti, Fe, Co, and Zr atoms with U_{eff} values of 3.0, 4.0, 3.3, and 3.0 eV, respectively.[21, 22] Upon optimized structures, the binding energies (BE) were calculated with eq. S4;

$$BE = E(\mathrm{PCP}\cdot n\mathrm{C_3H_4})_{eq}/n - E(\mathrm{PCP})_{eq}/n - E(\mathrm{G})_{eq} \qquad \text{(S4)}$$

where $E(\mathrm{PCP}\cdot n\mathrm{C_3H_4})_{eq}$ is the total energy of PCPs with *n* gas molecules per unit cell, $E(\mathrm{PCP})_{eq}$ and $E(\mathrm{G})_{eq}$ are the total energies of empty PCPs in the closed phase and one free gas molecule, respectively, and the subscript "eq" represents the equilibrium structure. Because the closed phases of these PCPs are difficult to obtain in experiment, we started from the reported analogy of these PCPs and replaced the corresponding atoms with Fe/Co and Ti/Zr, respectively. The structures of open phases of PCPs were taken from our experimental results.

Table S1. Crystal information of **NTU-65-series**

	NTU-65-FeZr	**NTU-65-FeTi**	**NTU-65-CoZr**	**NTU-65-CoTi**
Empirical formula	C_{24} H_{20} Fe F_6 N_8 Zr	C_{24} H_{20} Fe F_6 N_8 Ti	C_{24} H_{20} Co F_6 N_8 Zr	C_{24} H_{20} Co F_6 N_8 Ti
Formula weight	681.55	638.20	684.63	641.31
Crystal system	monoclinic	monoclinic	monoclinic	monoclinic
Space group	$P2_1/c$	$C\ 2/m$	$P2_1/c$	$P2_1/c$
Unit cell dimensions (Å)	a =13.709(8) b =25.837(15) c =12.830(8) β =117.798(7)	a =12.599(6) b =25.838(11) c =13.639(6) β =116.756(5)	a =13.517(16) b =25.270(3) c =12.693(15) β =117.986(16)	a =13.667(8) b =25.634(14) c =12.720(7) β =115.987(8)
Volume (Å^3)	4020(4)	3965(3)	3829(8)	4006(4)
Z	4	4	4	4
Density (calculated) (g/cm^3)	1.126	1.069	1.188	1.063
Mu (MoKa) (mm^{-1})	0.711	0.711	0.711	0.711
$F_{(000)}$	1360	1288	1364	1292
Theta min-max	2.926, 27.812	2.979, 28.367	1.611, 24.549	1.589, 25.099
Index ranges	-15<=h<=11 -29<=k<=25 -14<=l<=14	-9<=h<=16 -32<=k<=34 -18<=l<=18	-15<=h<=14 -29<=k<=29 -14<=l<=10	-16<=h<=15 -30<=k<=28 -15<=l<=15
Tot , Uniq Data, R(int)	16998, 5968, 0.131	11793, 4959, 0.085	17589, 6235, 0.113	29051, 7125, 0.095
Observed data [I > 2σ (I)]	3282	2630	3123	3638
Nref, Npar	5968, 362	4959, 183	6235, 361	7125, 361
R_1, wR_2, S	0.1491, 0.3762, 1.08	0.0835, 0.2385, 1.04	0.0775, 0.1684, 1.02	0.0591, 0.1635, 1.01
Max Shift	0	0	0	0

$R = \Sigma||F_o|-|F_c||/\Sigma|F_o|$, $wR = \{\Sigma[w\,(|F_o|^2 - |F_c|^2)^2]/\Sigma[w\,(|F_o|^4)]\}^{/2}$ and $w = 1/[\sigma^2(F_o^2) + (0.1452P)^2]$

where $P = (F_o^2+2F_c^2)/3$

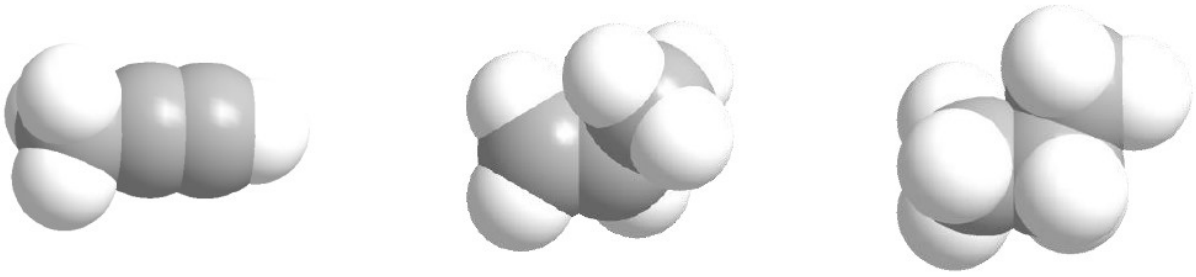

Figure S1. Comparison of the molecular size and shape of C_3H_4, C_3H_6 and C_3H_8.

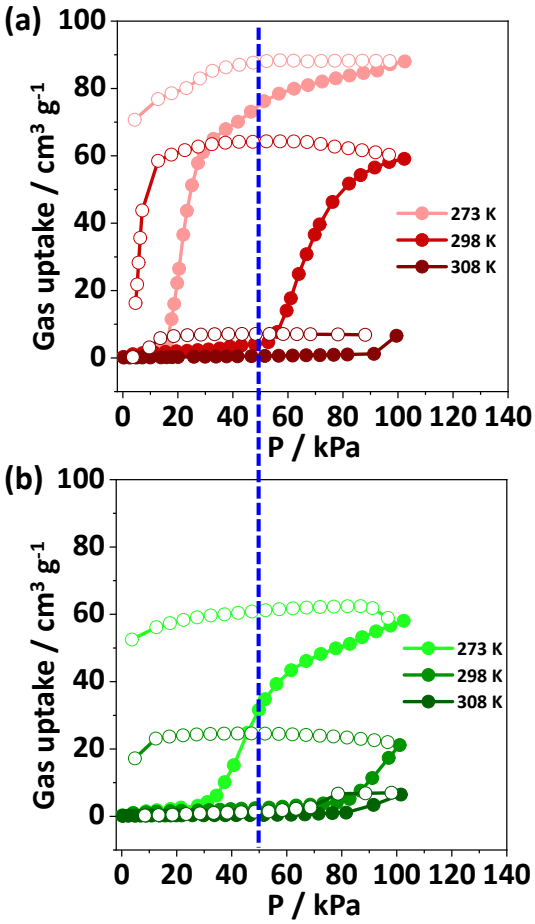

Figure S2. Single-component C_3H_6 (a) and C_3H_8 (b) isotherms of **NTU-65** at different temperatures.

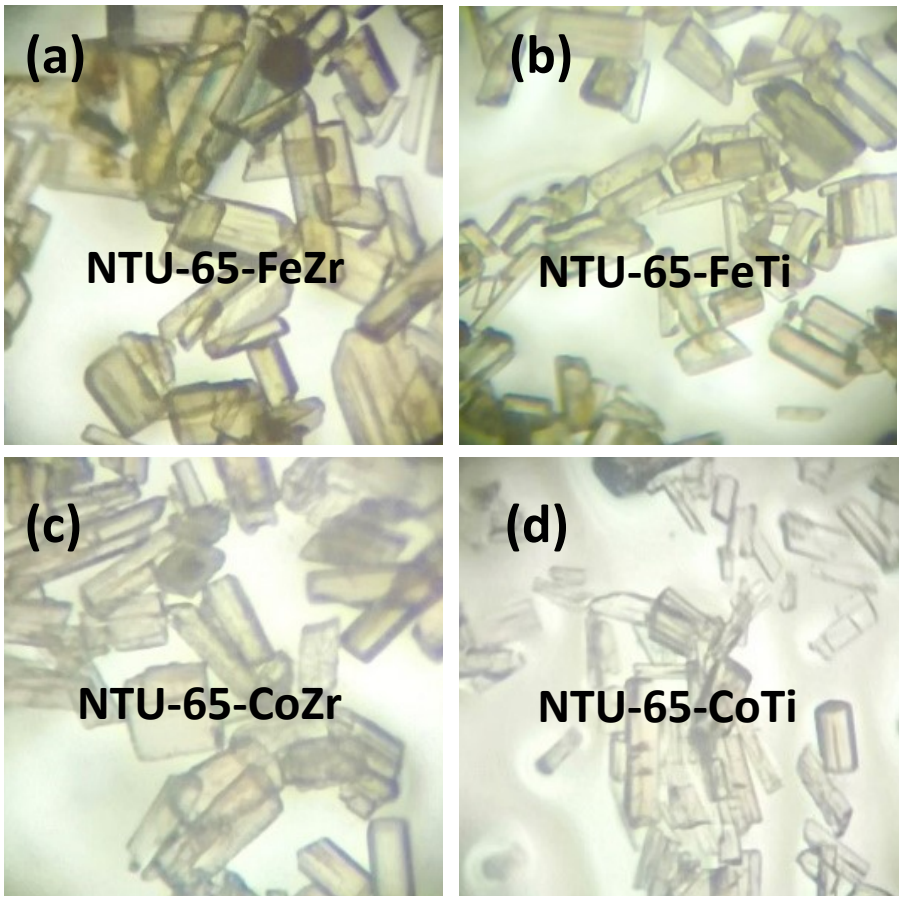

Figure S3. Photos of **NTU-65-series**.

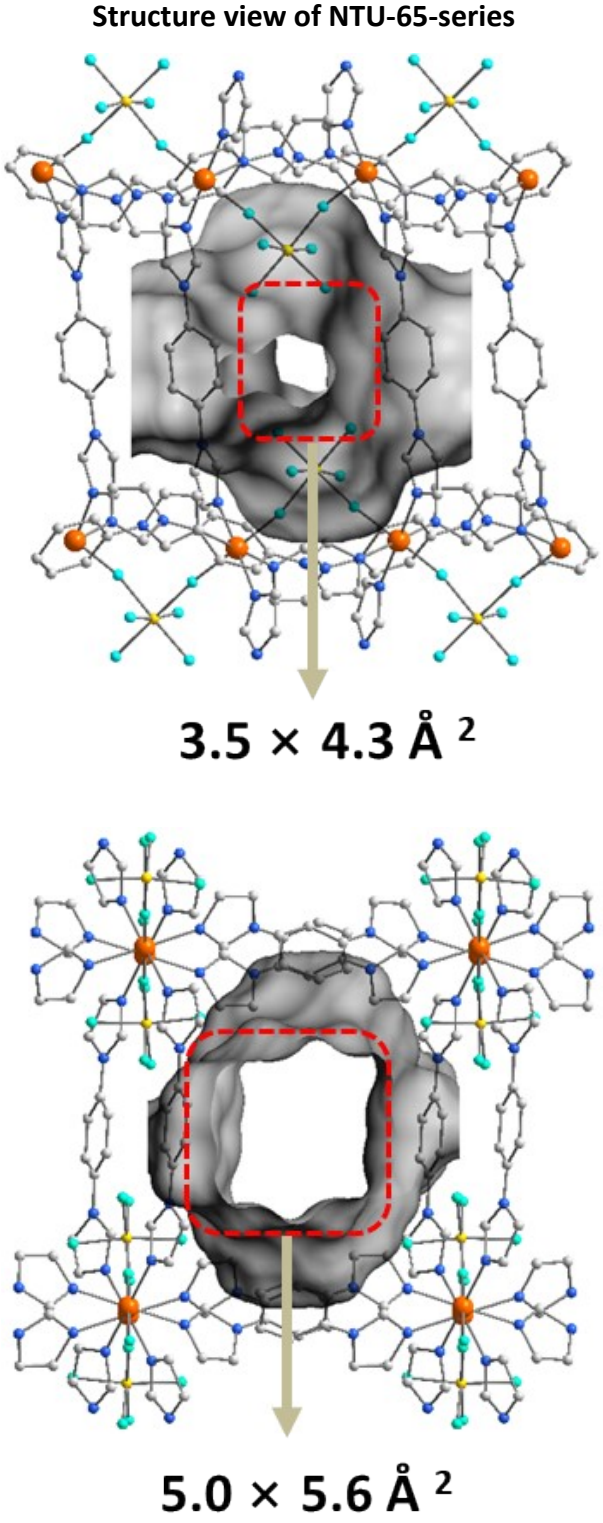

Figure S4. Two kinds of channels in **NTU-65-FeZr**, where the accessible nanospace was highlighted by gray.

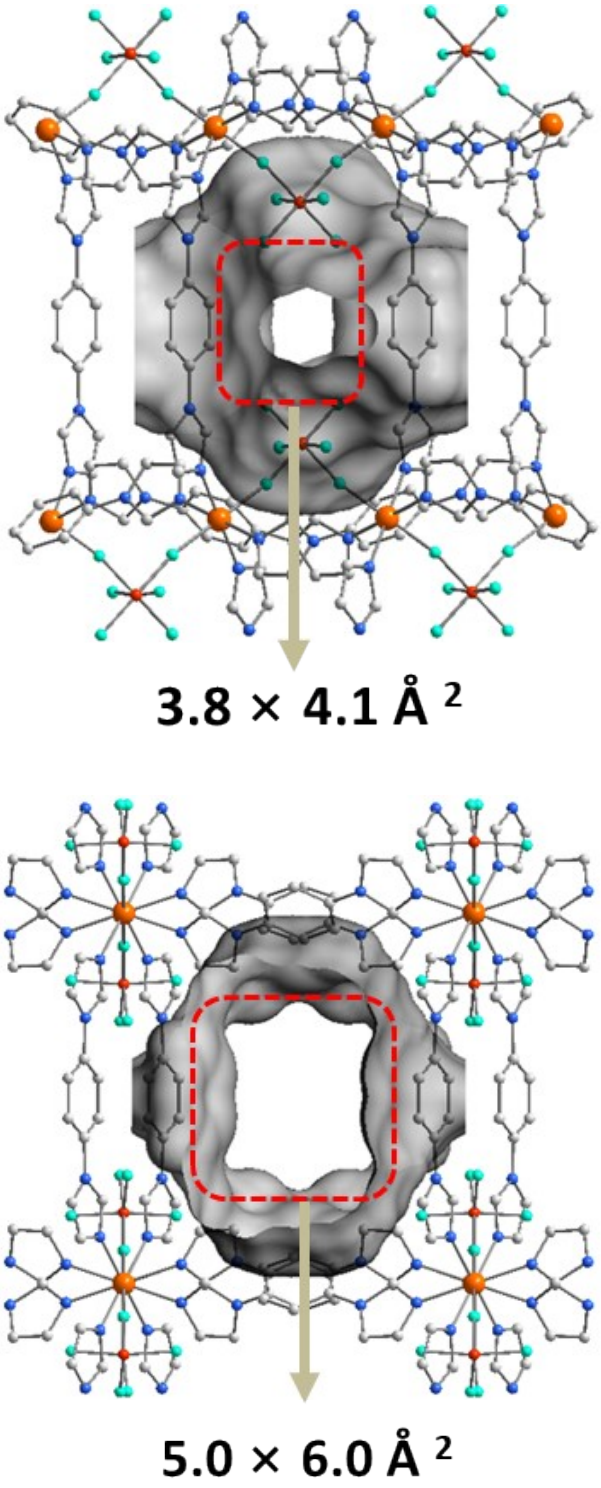

Figure S5. Two kinds of channels in **NTU-65-FeTi**, where the accessible nanospace was highlighted by gray.

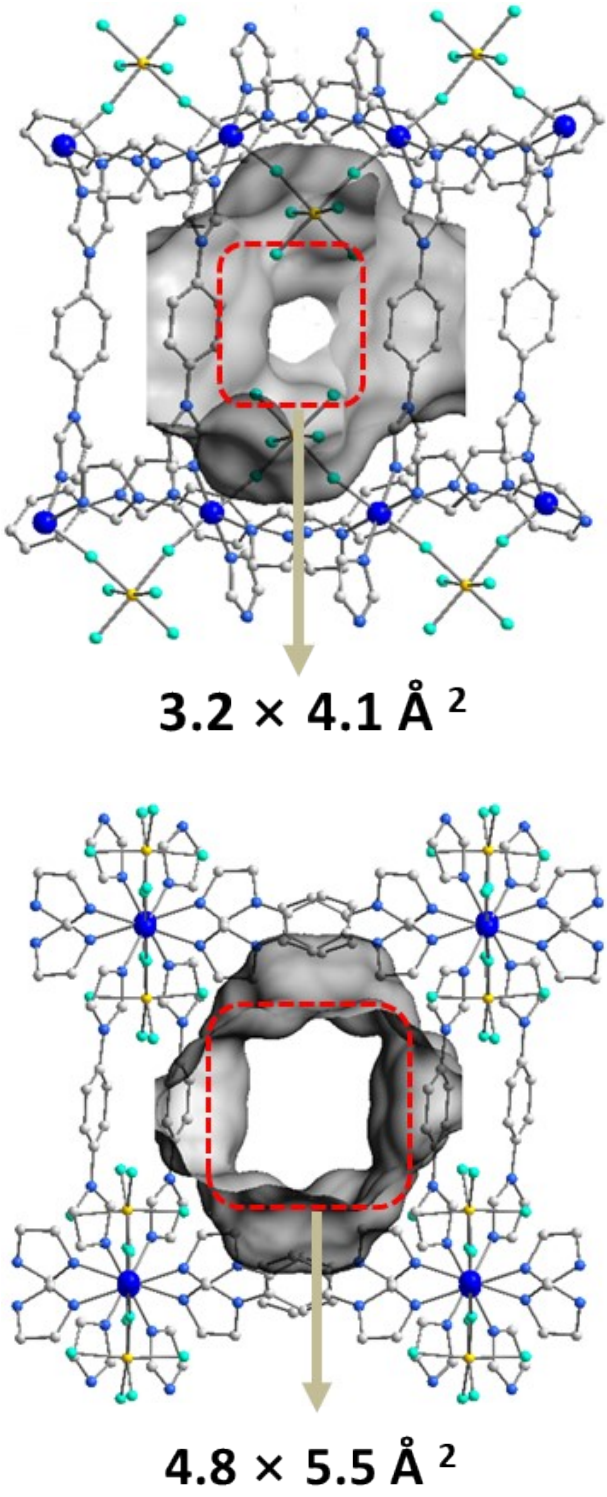

Figure S6. Two kinds of channels in **NTU-65-CoZr**, where the accessible nanospace was highlighted by gray.

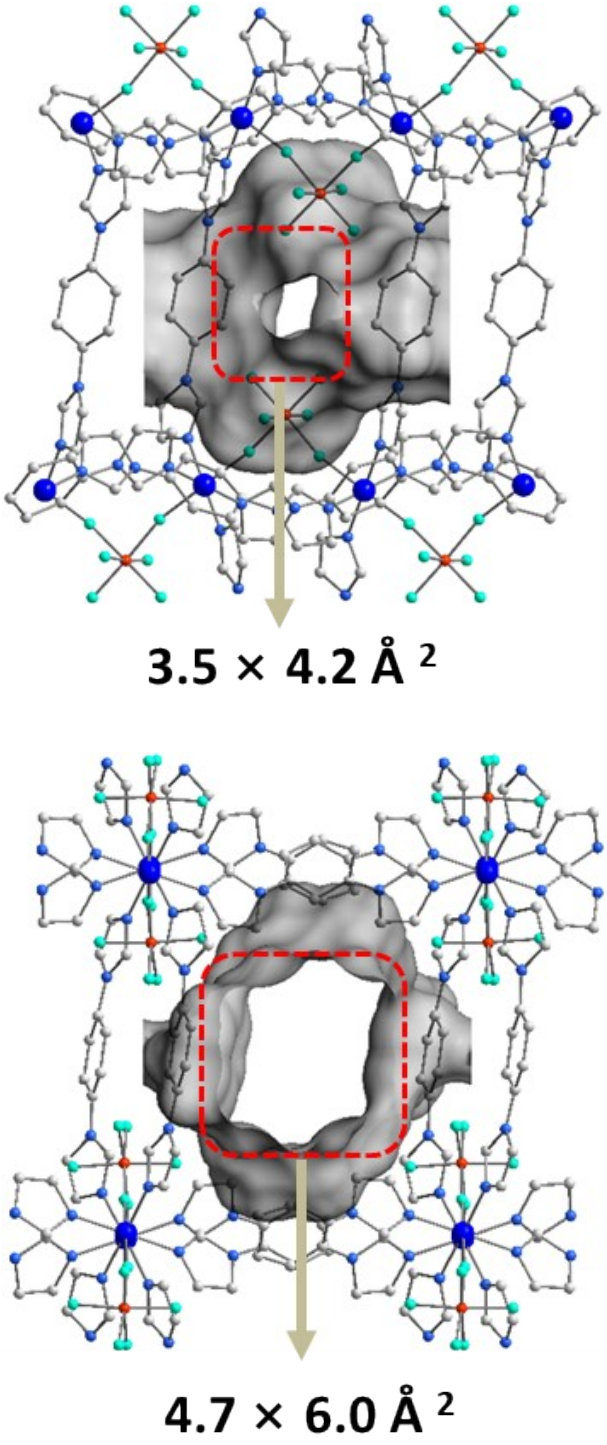

Figure S7. Two kinds of channels in **NTU-65-CoTi**, where the accessible nanospace was highlighted by gray.

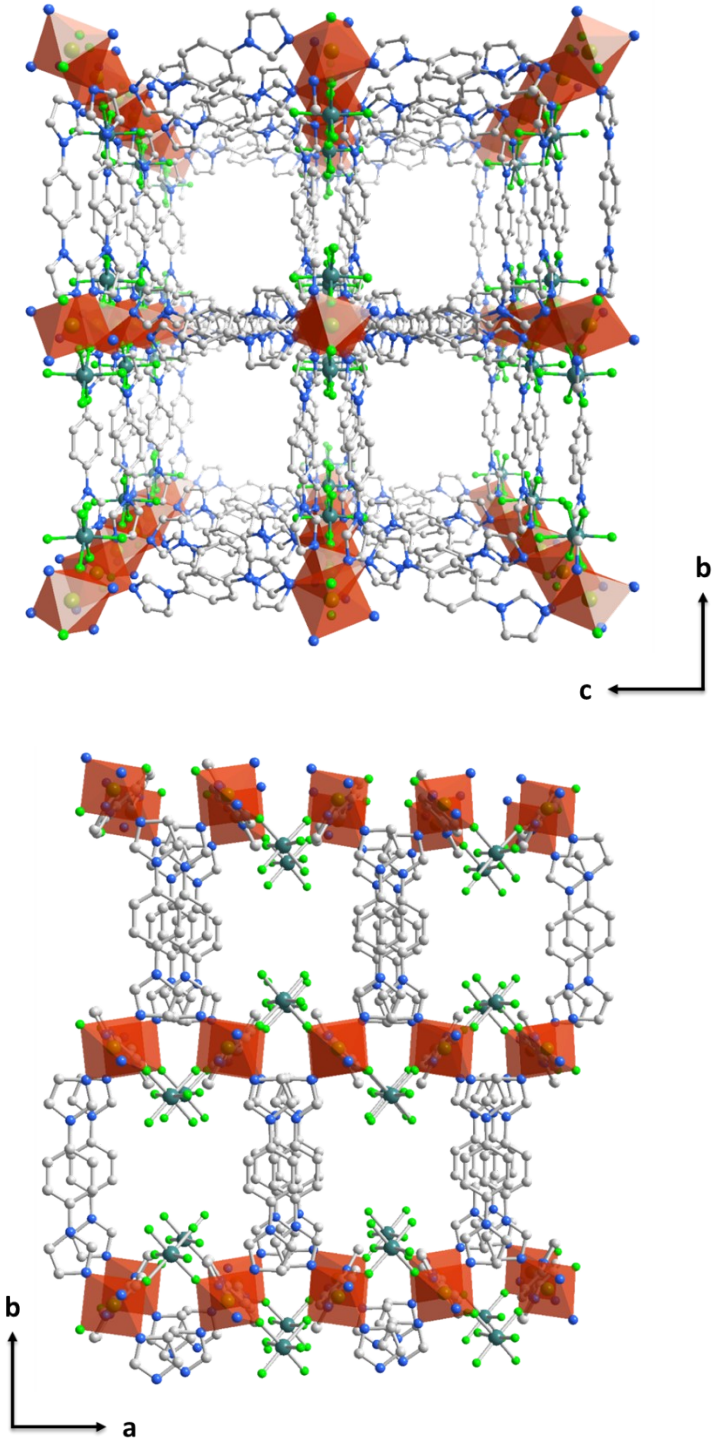

Figure S8. Packing view of the as-synthesized **NTU-65-series** framework along different directions.

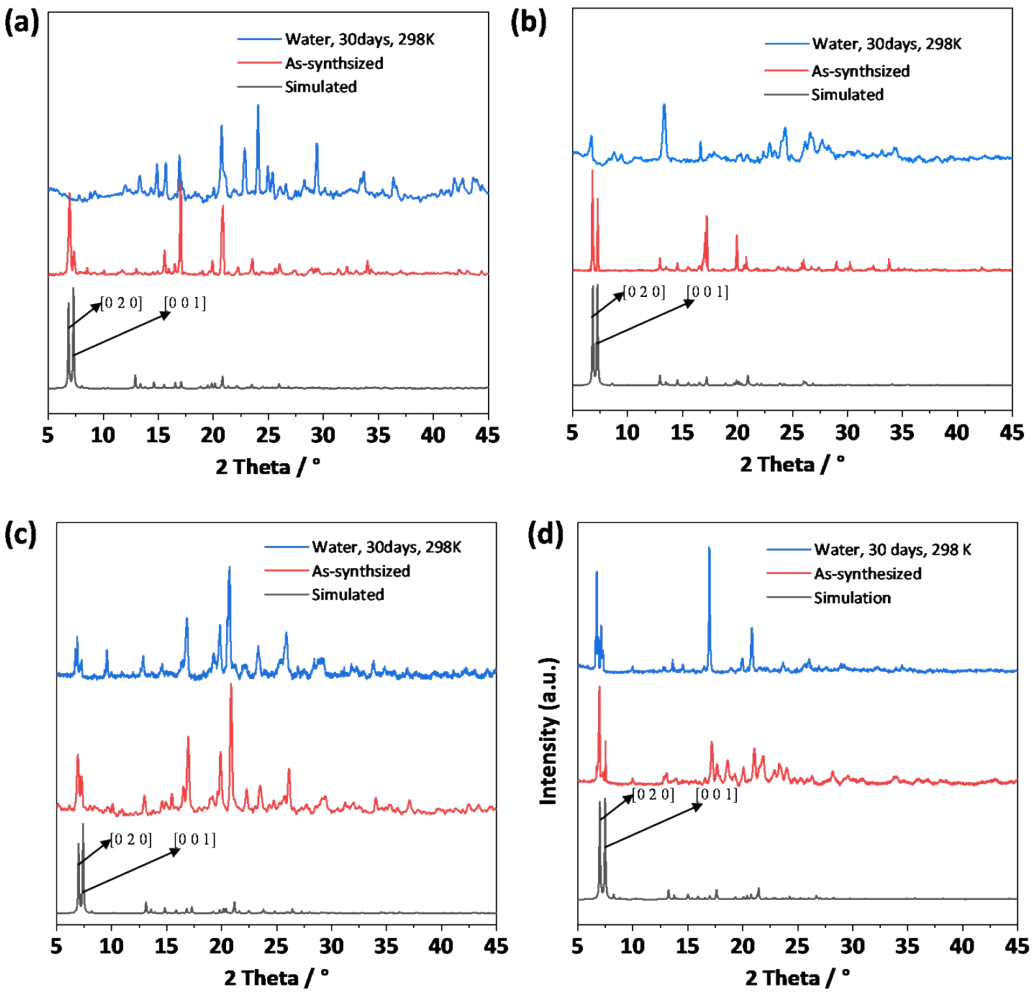

Figure S9. PXRD patterns of **NTU-65-FeZr** (a), **NTU-65-FeTi** (b), **NTU-65-CoZr** (c) and **NTU-65-CoTi** (d): simulated, as-synthesized and soak in water for 30 days at 298 K samples. Phase purity of the bulk crystals was identified by a comparison of the experimental and simulated patterns. The activated phases are still high crystalline materials, and only the position of some diffraction peaks has shifted, indicating structural change after solvent removal.

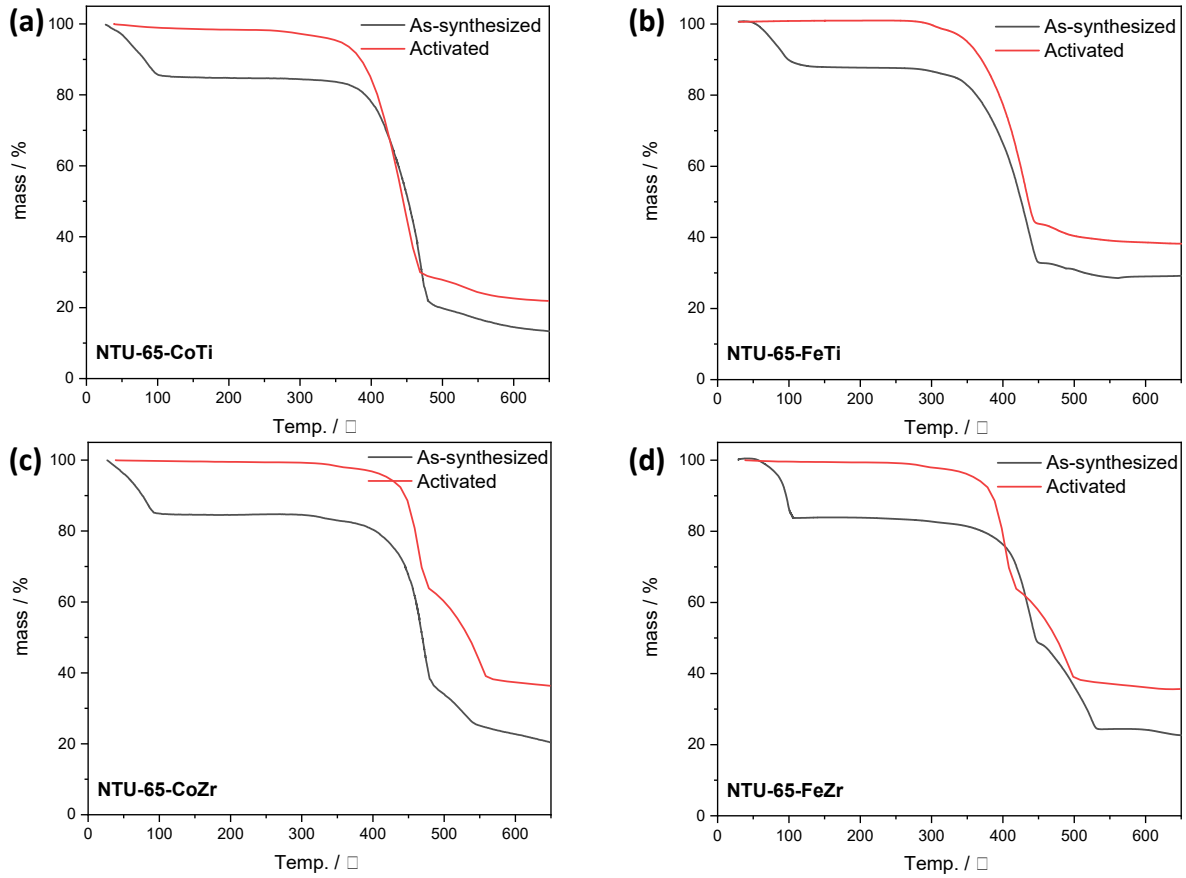

Figure S10. TG curves of **NTU-65-FeZr** (a), **NTU-65-FeTi** (b), **NTU-65-CoZr** (c) and **NTU-65-CoTi** (d).

According to these results, activated phases of the four MOFs can be obtained by degassing methanol exchanged crystals under high vacuum at 120 °C for 20 h.

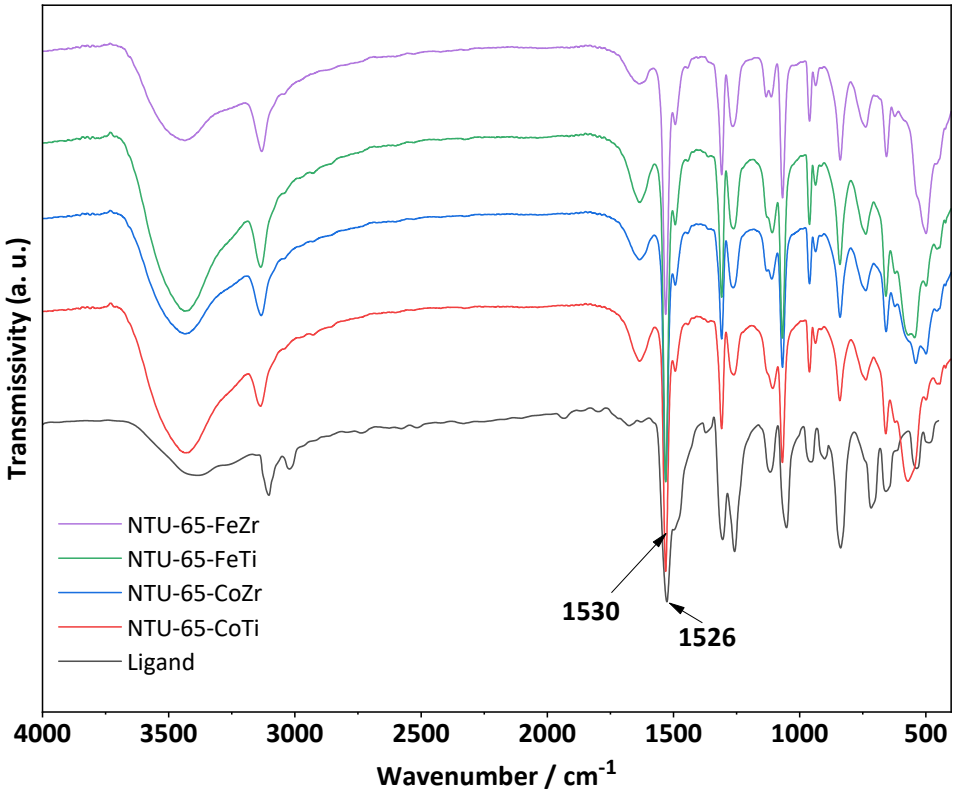

Figure S11. Infrared spectra of ligand and **NTU-65-series**.

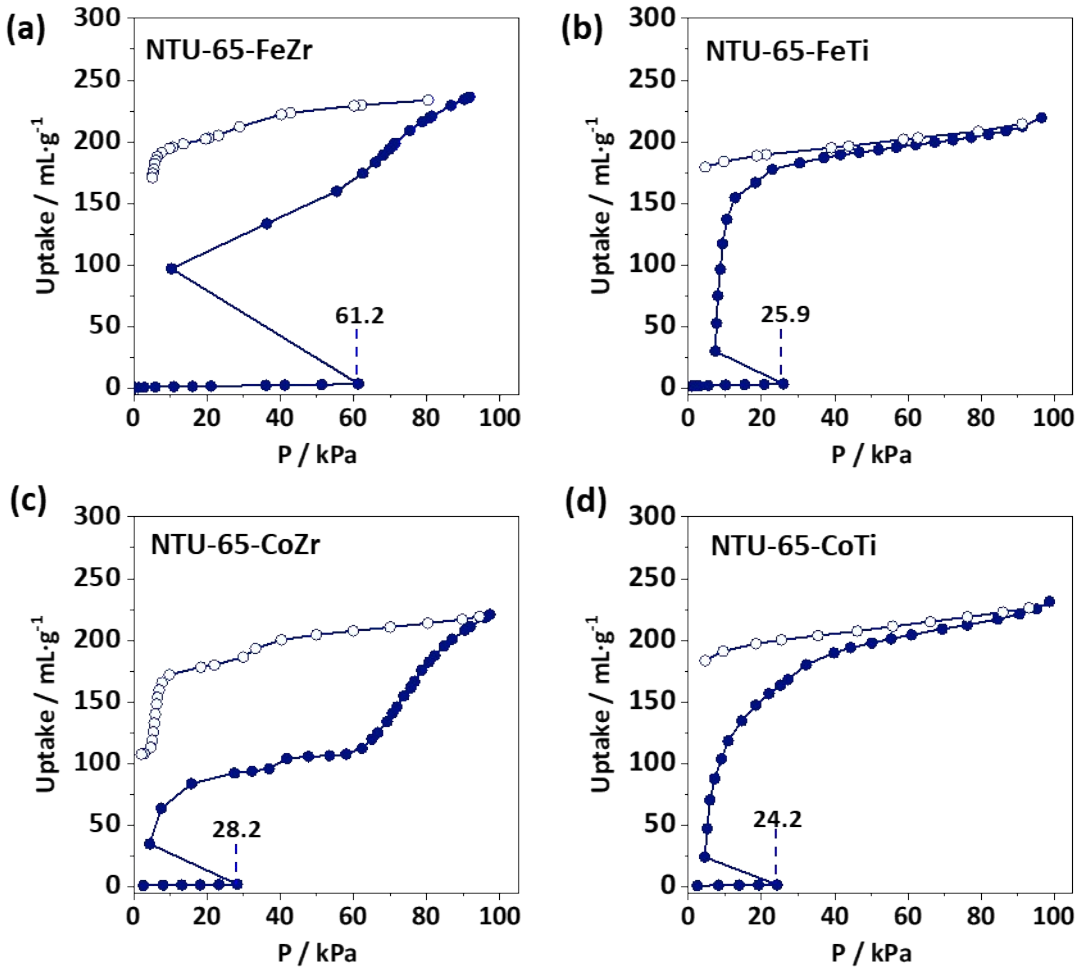

Figure S12. N_2 adsorption isotherms of **NTU-65-series** at 77 K. A 'kink' phenomenon occurred on all of them. Compared to the polar N_2 probe (77 K), CO_2 molecule with large quadrupole-moment (-13.4 × 10^{-40} C m^2) may interact with the electronegative F sites of the frameworks in a relatively strong manner. Therefore, the instantaneous gate-opening triggered by N_2 at 77 K may change to a gradual opening following an increase pressure of CO_2, yielding eliminated "kink" phenomenon (Figure 2 in draft).

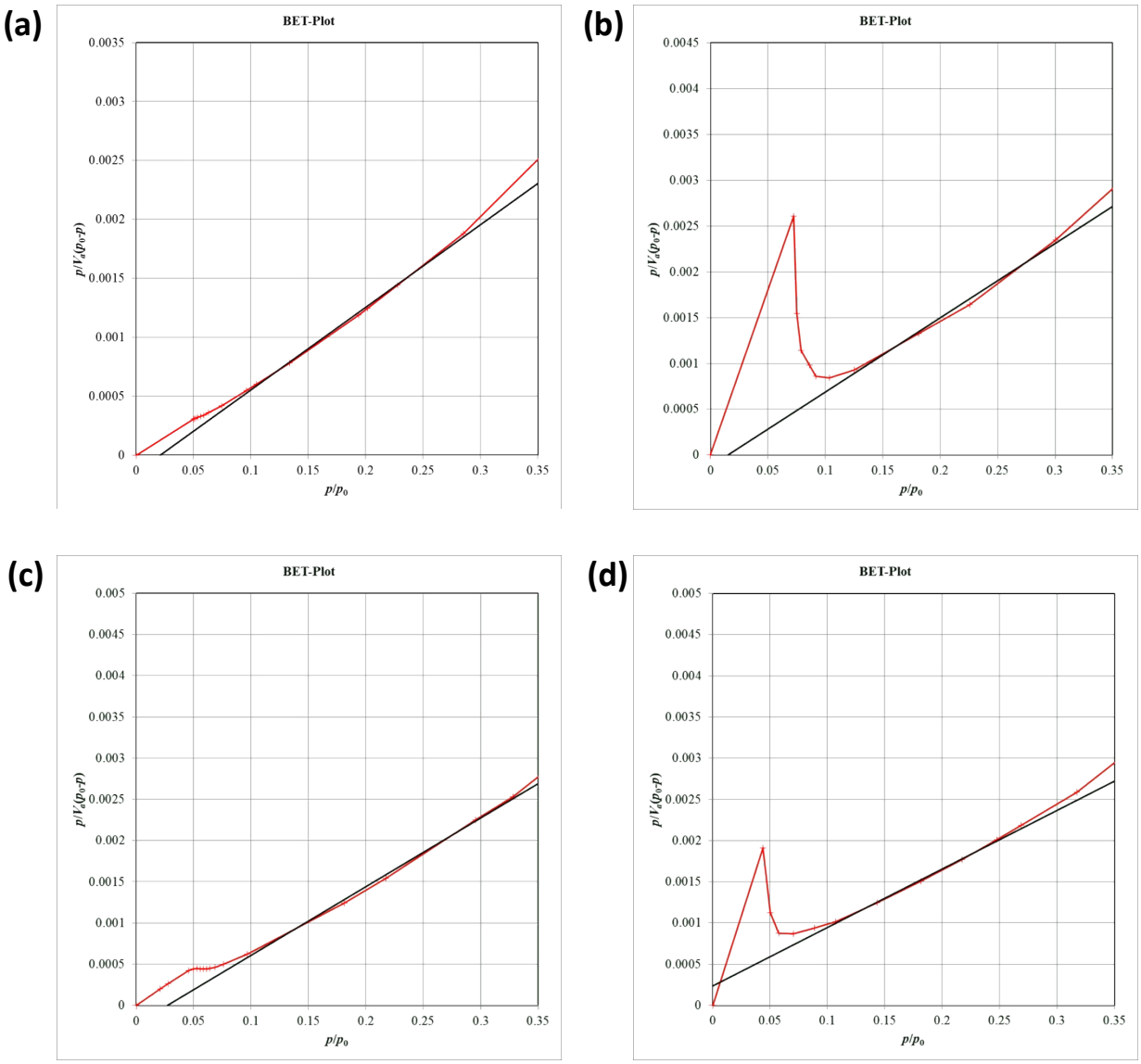

Figure S13. The consistency plots for BET fitting for **NTU-65-FeZr** (a), **NTU-65-FeTi** (b), **NTU-65-CoZr** (c) and **NTU-65-CoTi** (d).

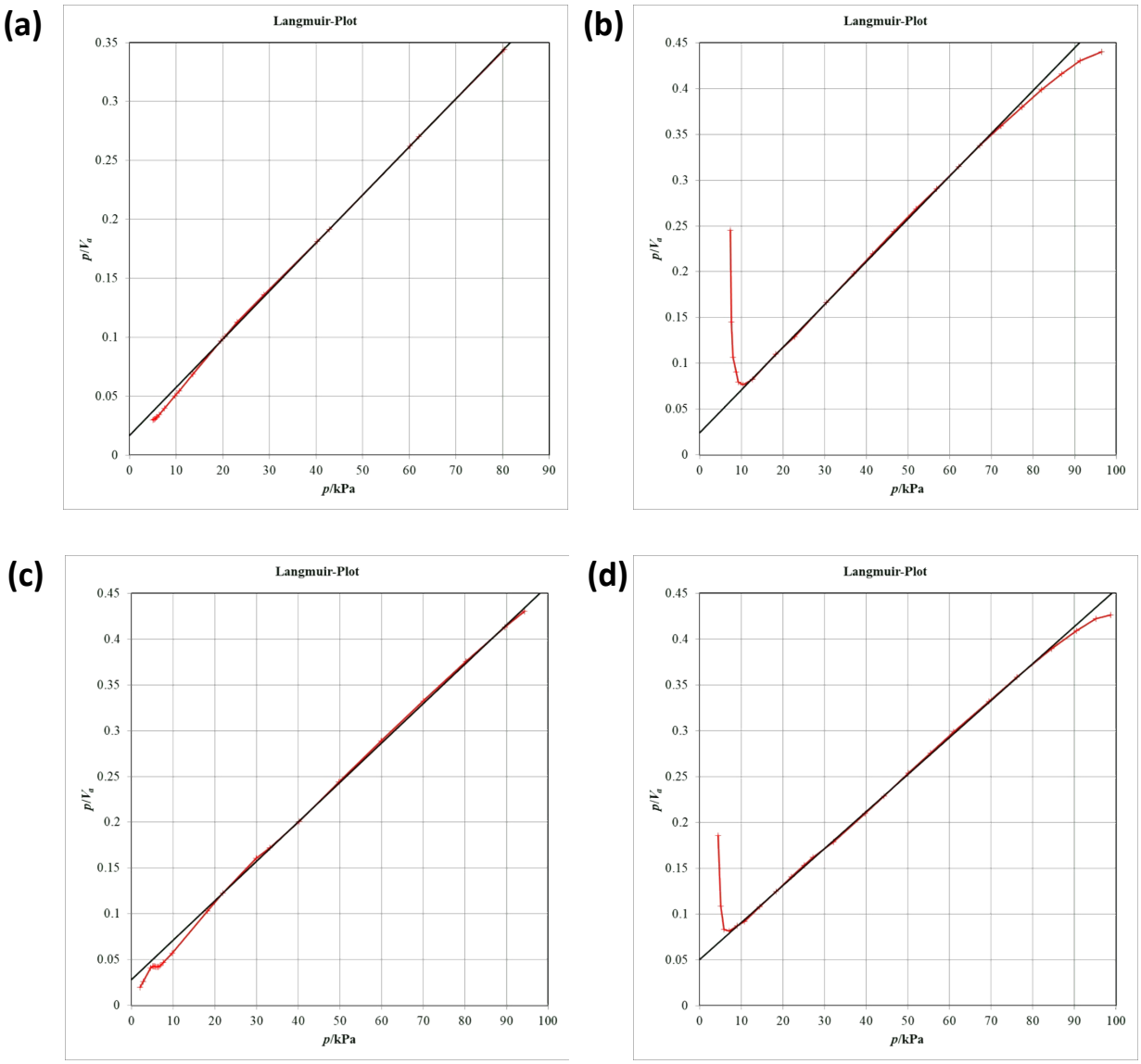

Figure S14. The consistency plots for Langmuir fitting for **NTU-65-FeZr** (a), **NTU-65-FeTi** (b), **NTU-65-CoZr** (c) and **NTU-65-CoTi** (d).

Table S2. The specific surface area and pore volume of **NTU-65-series**.

Materials	**S_{BET} ($m^2 \cdot g^{-1}$)**	**$S_{Langmuir}$ ($m^2 \cdot g^{-1}$)**	**V_t ($cm^3 \cdot g^{-1}$)**
NTU-65-FeZr	635.0	1066.1	0.3615
NTU-65-FeTi	545.3	931.8	0.3395
NTU-65-CoZr	537.3	1011.9	0.3392
NTU-65-CoTi	592.7	1078.5	0.3579

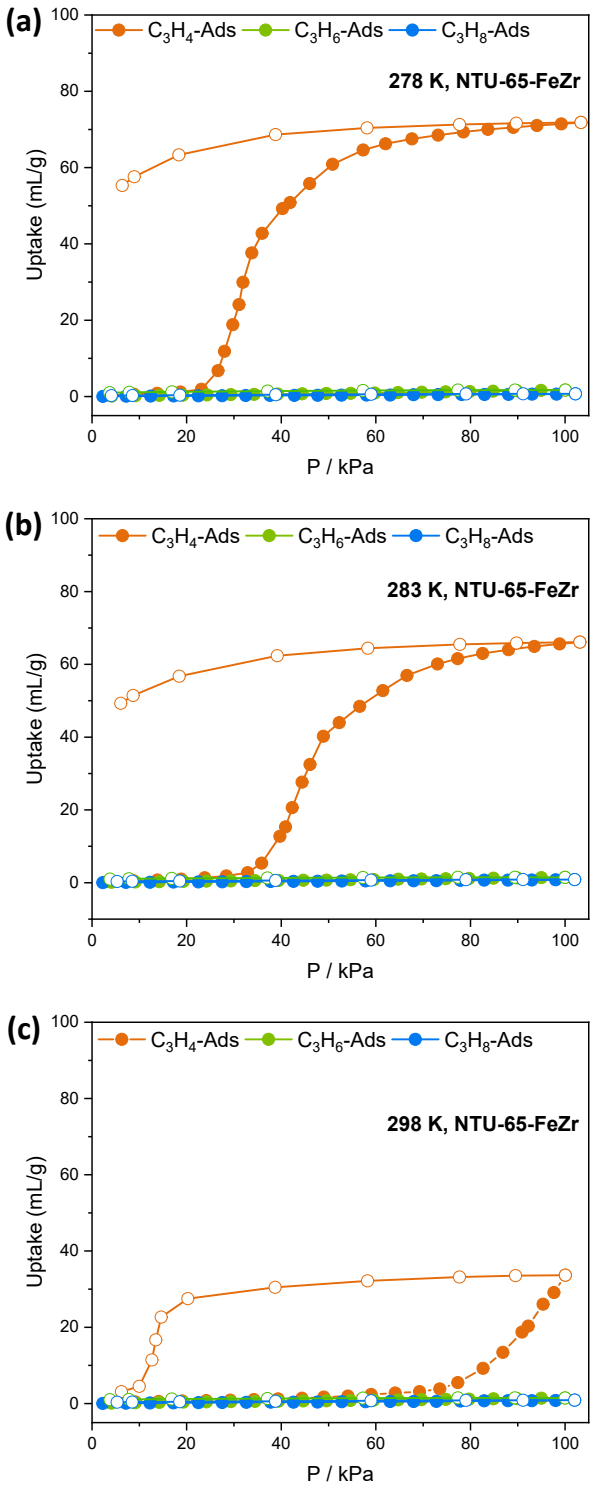

Figure S15. Single-component C_3H_4, C_3H_6 and C_3H_8 isotherms of **NTU-65-FeZr** at 278 (a), 283 (b), and 298 K (c). Following increased temperature, the gate-opening of C_3H_4 becomes late, however, both C_3H_6 and C_3H_8 can not open the framework threshold the pressure under these temperatures.

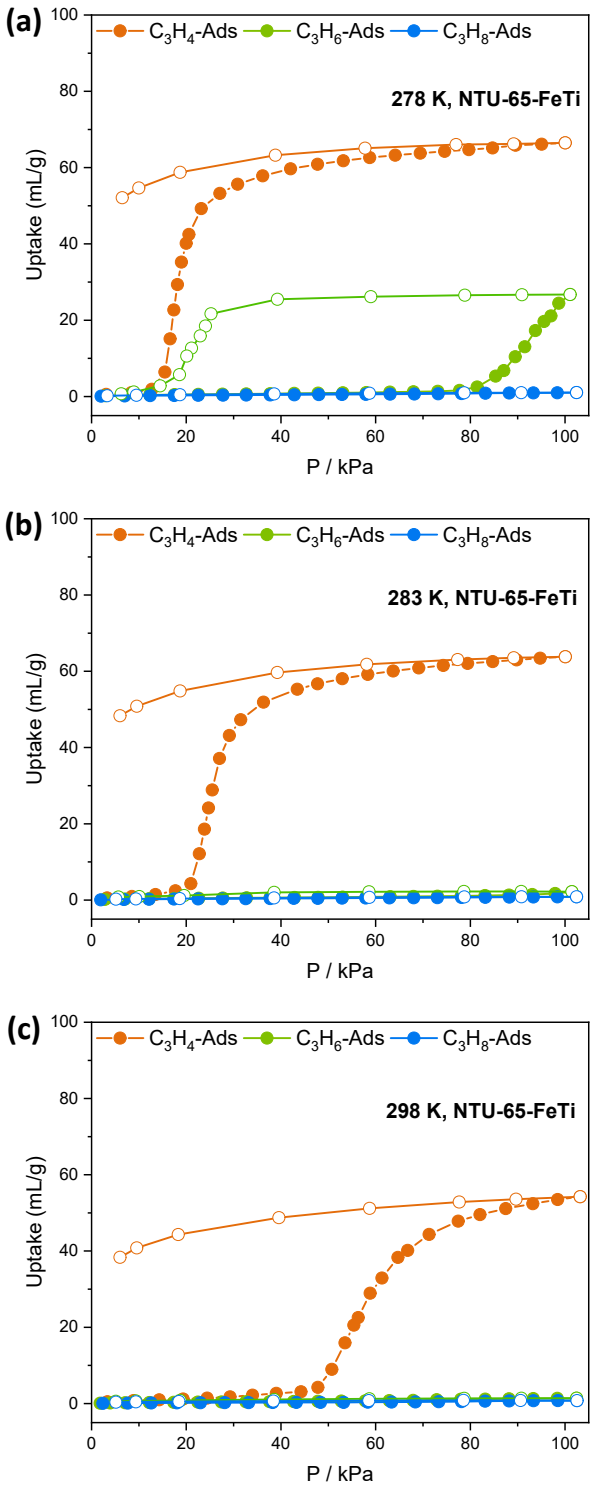

Figure S16. Single-component C_3H_4, C_3H_6 and C_3H_8 isotherms of **NTU-65-FeTi** at 278 (a), 283 (b), and 298 K (c). Following increased temperature, the gate-opening of C_3H_4 becomes late, while the gate-opening only occurs at the temperature < 278 K toward C_3H_6. However, C_3H_8 can not open the framework threshold the pressure under these temperatures.

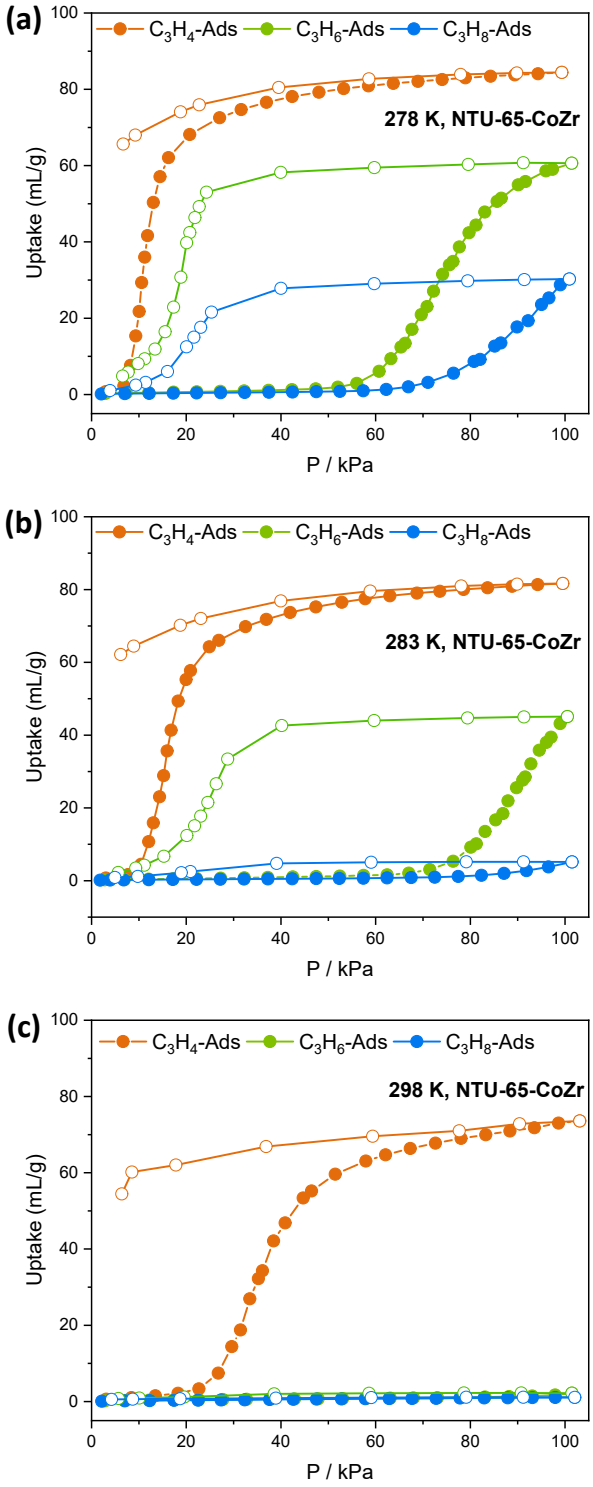

Figure S17. Single-component C_3H_4, C_3H_6 and C_3H_8 isotherms of **NTU-65-CoZr** at 278 (a), 283 (b), and 298 K (c). Following increased temperature, the gate-opening of C_3H_4 becomes late, while the gate-opening only occurs at the temperature < 283 K toward C_3H_6. In addition, the gate-opening also occurs toward C_3H_8 when the temperature < 278 K.

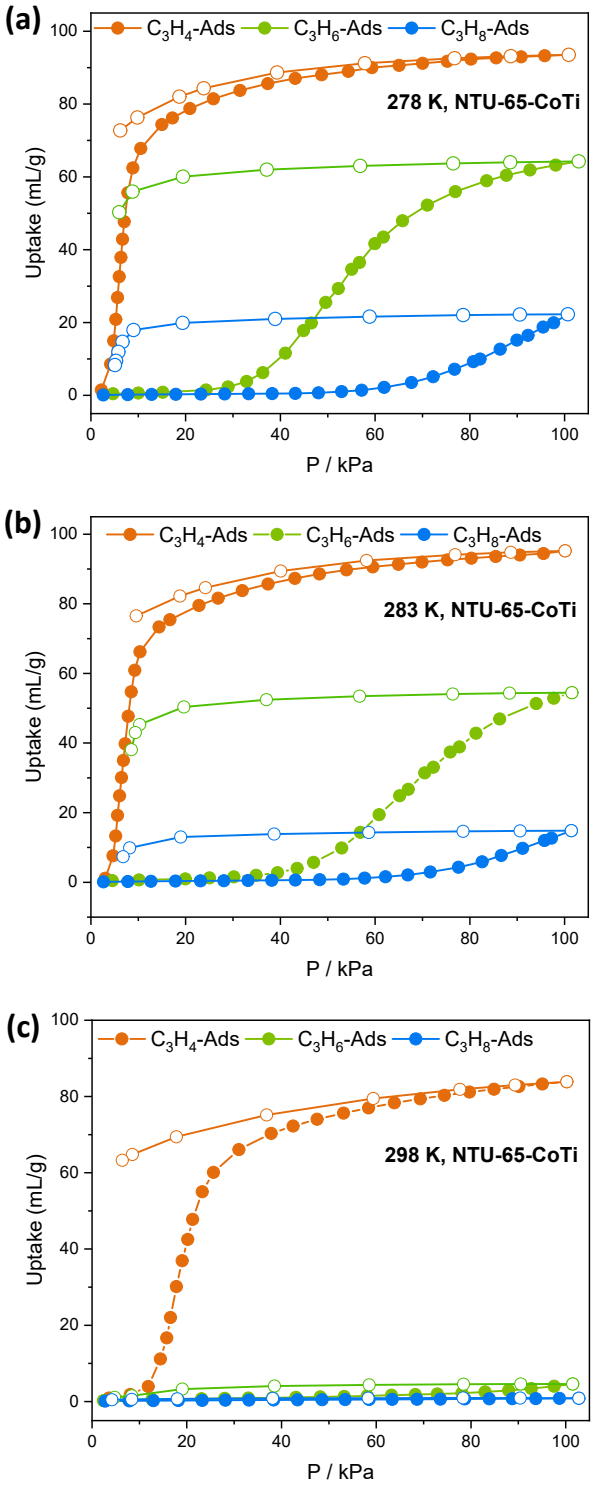

Figure S18. Single-component C_3H_4, C_3H_6 and C_3H_8 isotherms of **NTU-65-CoTi** at 278 (a), 283 (b), and 298 K (c). Following increased temperature, the gate-opening of C_3H_4 also becomes late, while the gate-opening only occurs at the temperature < 283 K toward C_3H_6 with advanced pressure. In addition, the gate-opening occurs toward C_3H_8 when the temperature < 283 K.

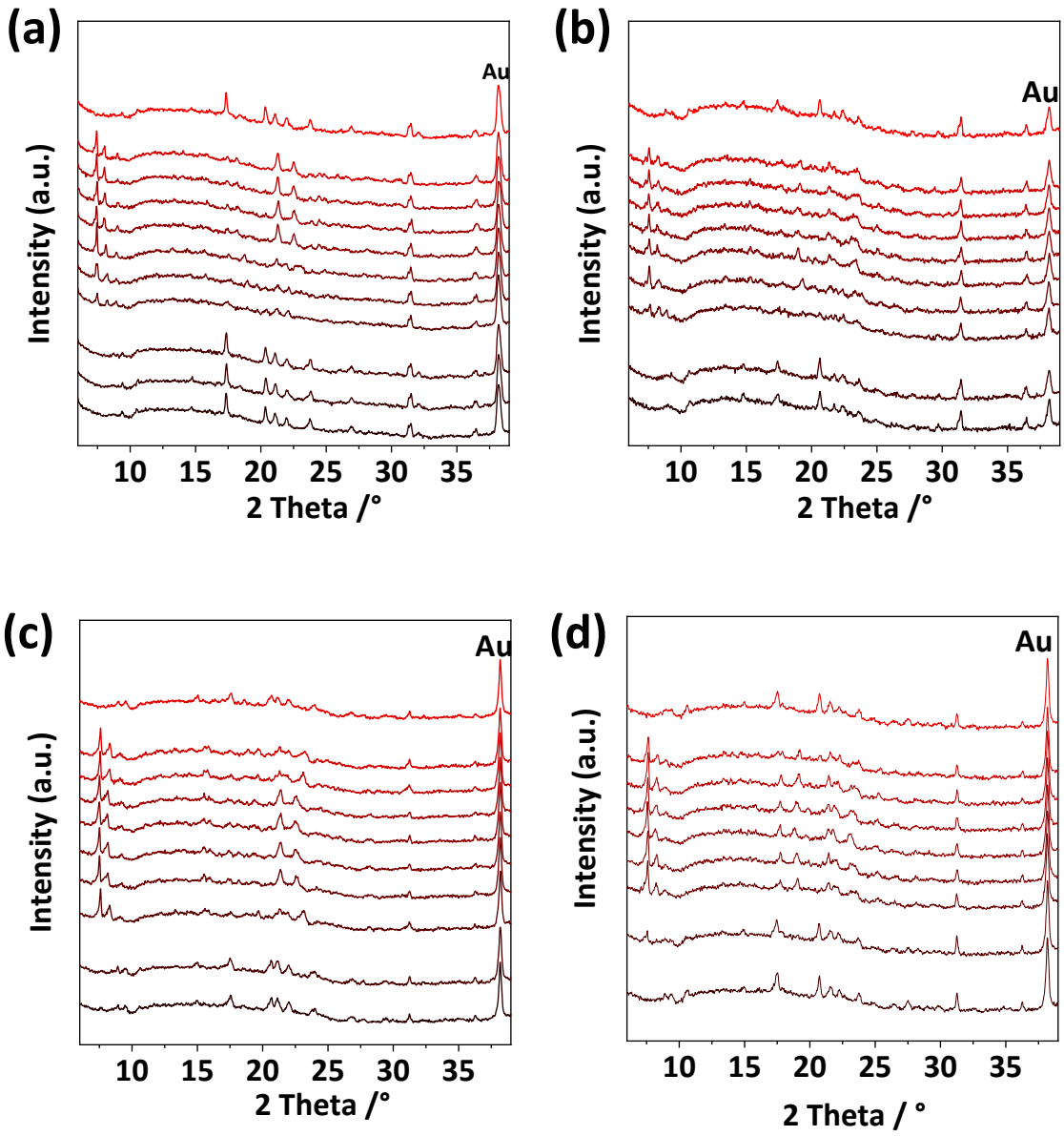

Figure S19. Coincident in-situ PXRD patterns of the four crystals (a: **NTU-65-FeZr**, b: **NTU-65-FeTi**, c: **NTU-65-CoZr**, d: **NTU-65-CoTi**) at given equilibrium pressures during C_3H_4 adsorption and desorption at 273 K. PXRD was collected after 20 min

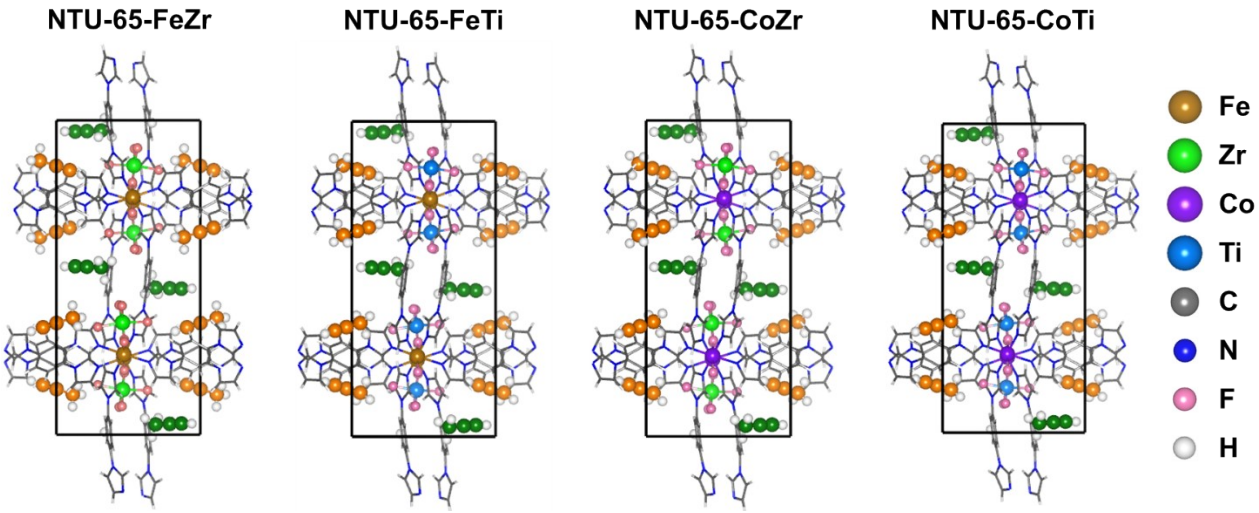

Figure S20. Optimized adsorption structures of C_3H_4 in **NTU-65-series**. The adsorption positions of C_3H_4 were obtained by canonical Monte-Carlo simulation followed by density functional theory calculations. There are two kinds of adsorption sites, each of which contains four symmetrical positions. As a result, a total of eight molecules per unit cell were considered to calculate the binding energy of C_3H_4 with these PCPs. This amount is very similar to the experimental result (once the gate-opening finish: 8.5) for C_3H_4 adsorption in **NTU-65-CoTi**.

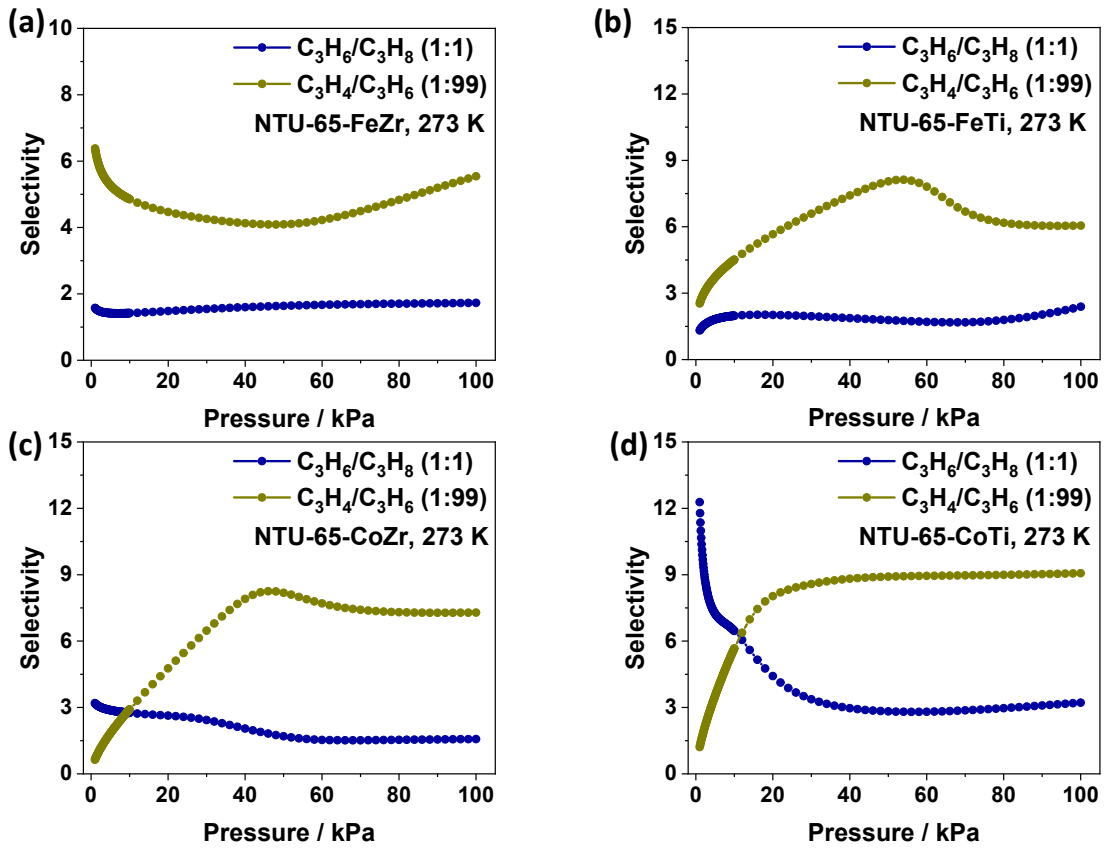

Figure S21. Calculated IAST selectivity for C_3H_4/C_3H_6 mixtures (v/v = 1/99) and C_3H_6/C_3H_8 mixtures (v/v = 1/1) at 273 K.

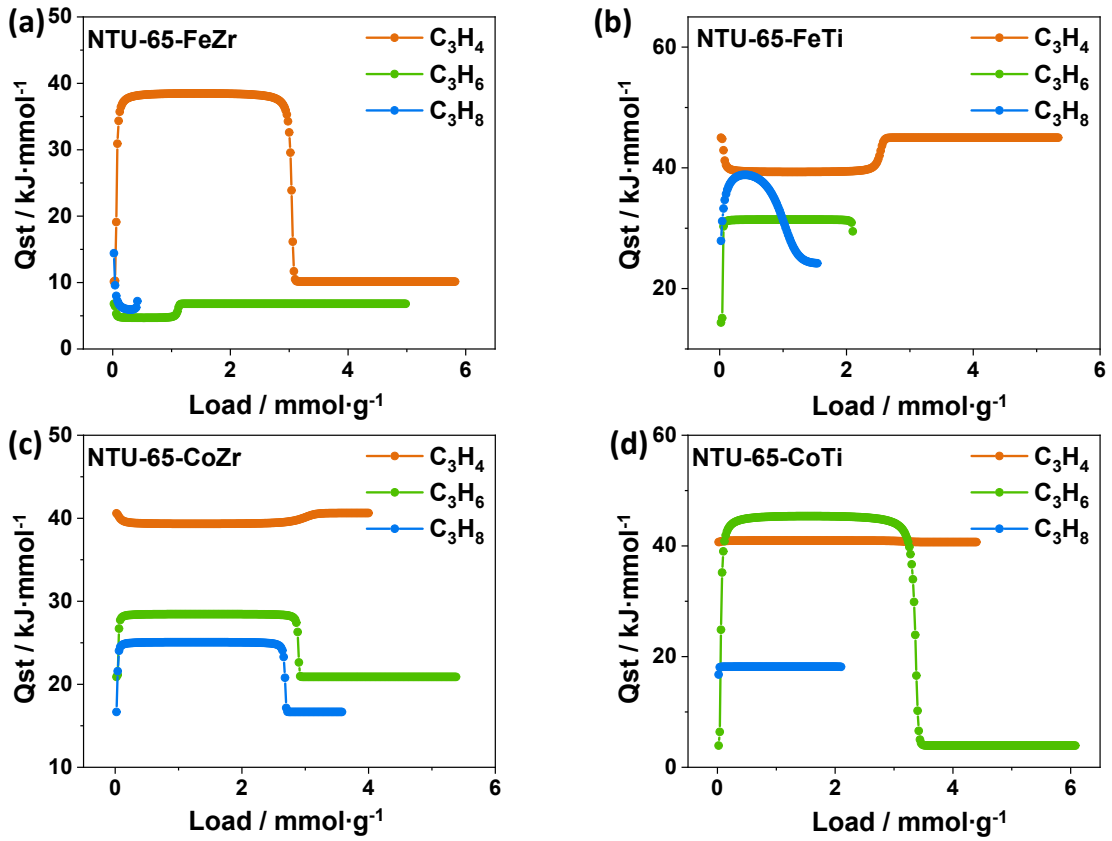

Figure S22. The calculated adsorption heats of C_3H_4, C_3H_6 and C_3H_8 in **NTU-65-series**.

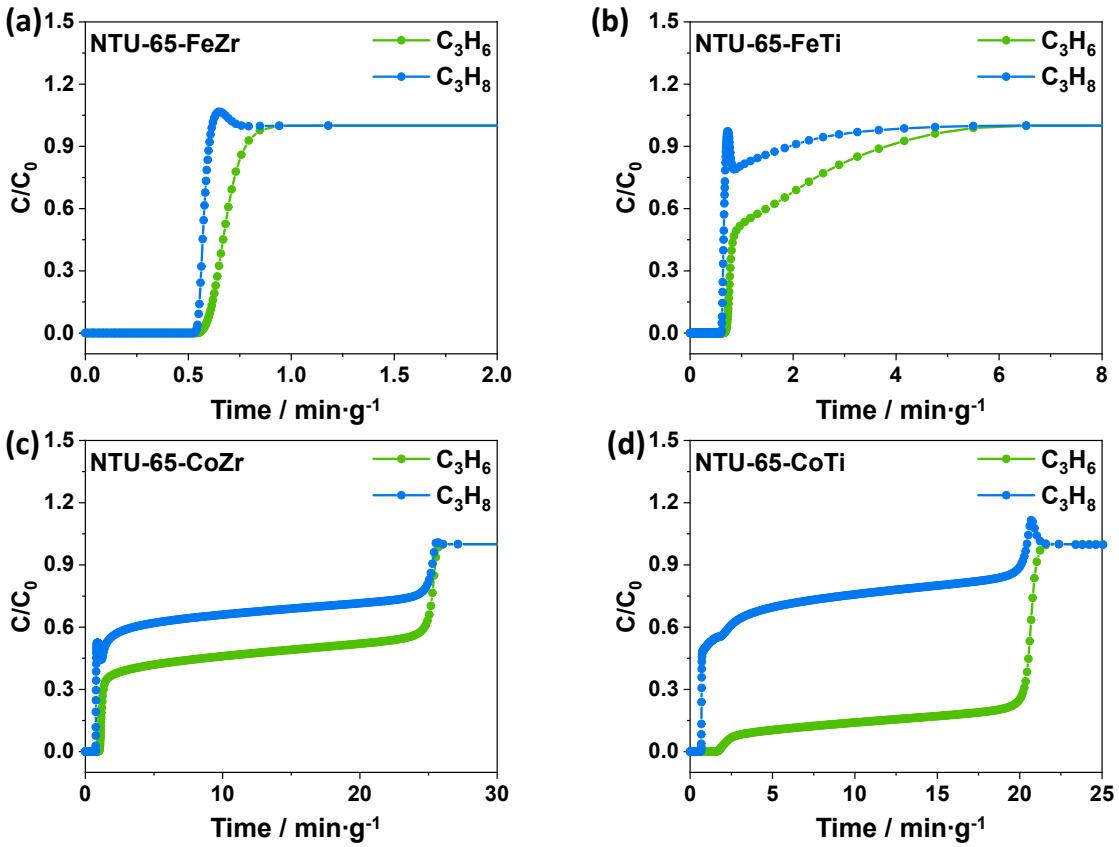

Figure S23. Calculated breakthrough curves for C_3H_6/C_3H_8 mixtures (v/v = 1/1) at 1 bar flowing through a fixed bed of **NTU-65-series** at 273 K.

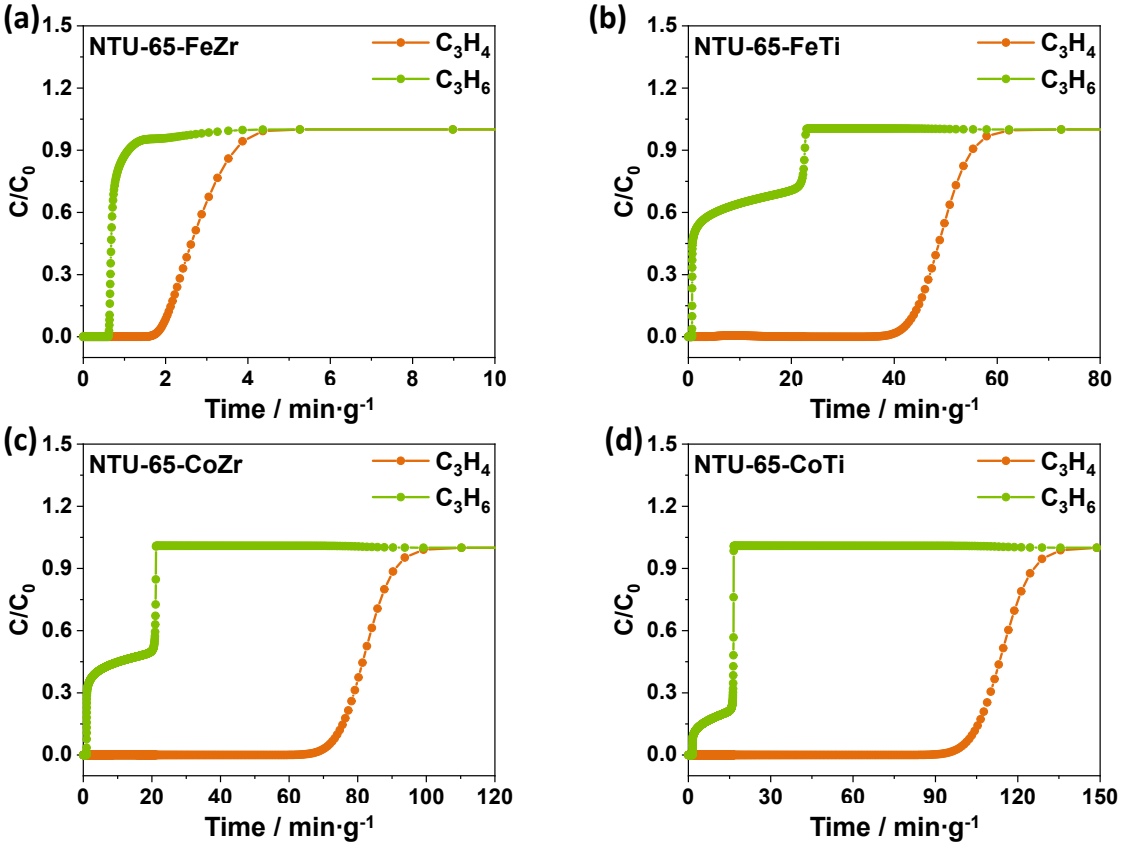

Figure S24. Calculated breakthrough curves for C_3H_4/C_3H_6 mixtures (v/v = 1/99) at 1 bar flowing through a fixed bed of **NTU-65-series** at 273 K.

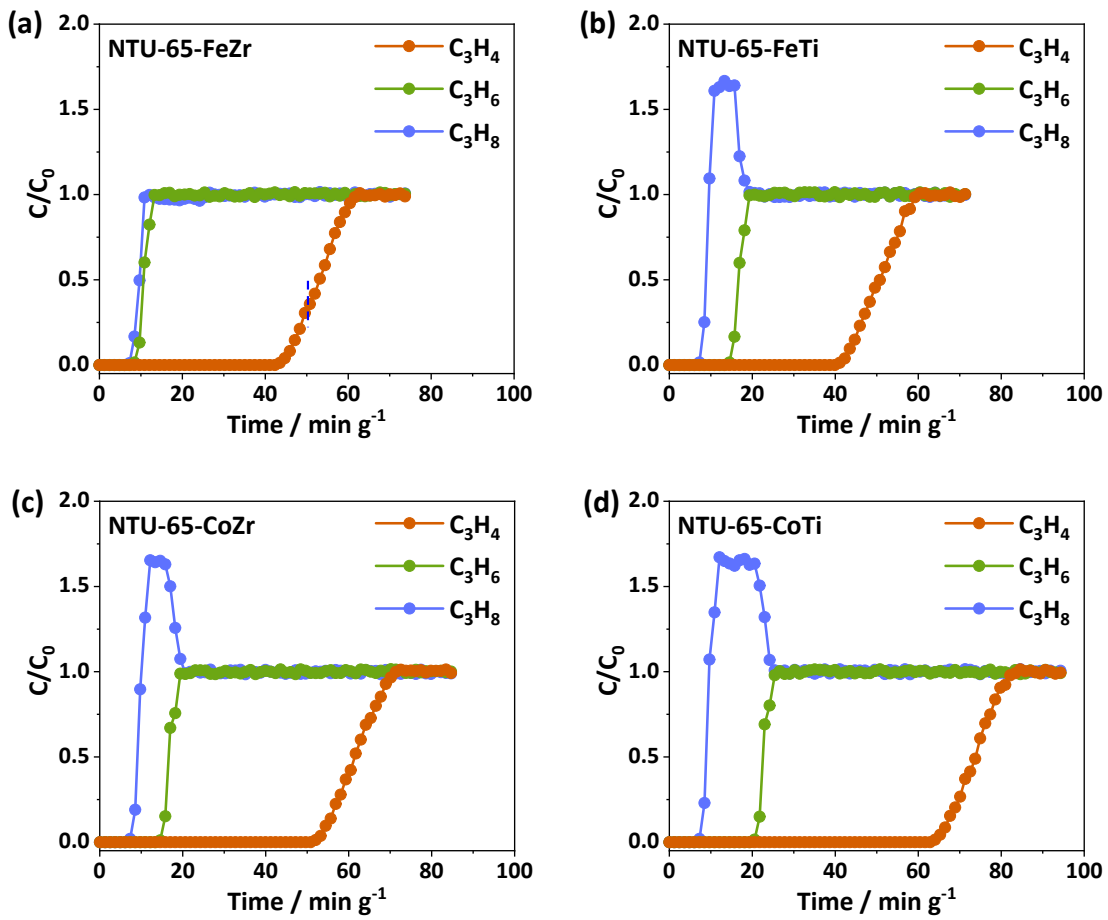

Figure S25. Experimental breakthrough curves of **NTU-65-FeZr** (a), **NTU-65-FeTi** (b), **NTU-65-CoZr** (c) and **NTU-65-CoTi** (d) for $C_3H_4/C_3H_6/C_3H_8$ (0.5/49.75/49.75, v/v/v) separation at 273 K (gas velocity: 5.0 mL·min^{-1}).

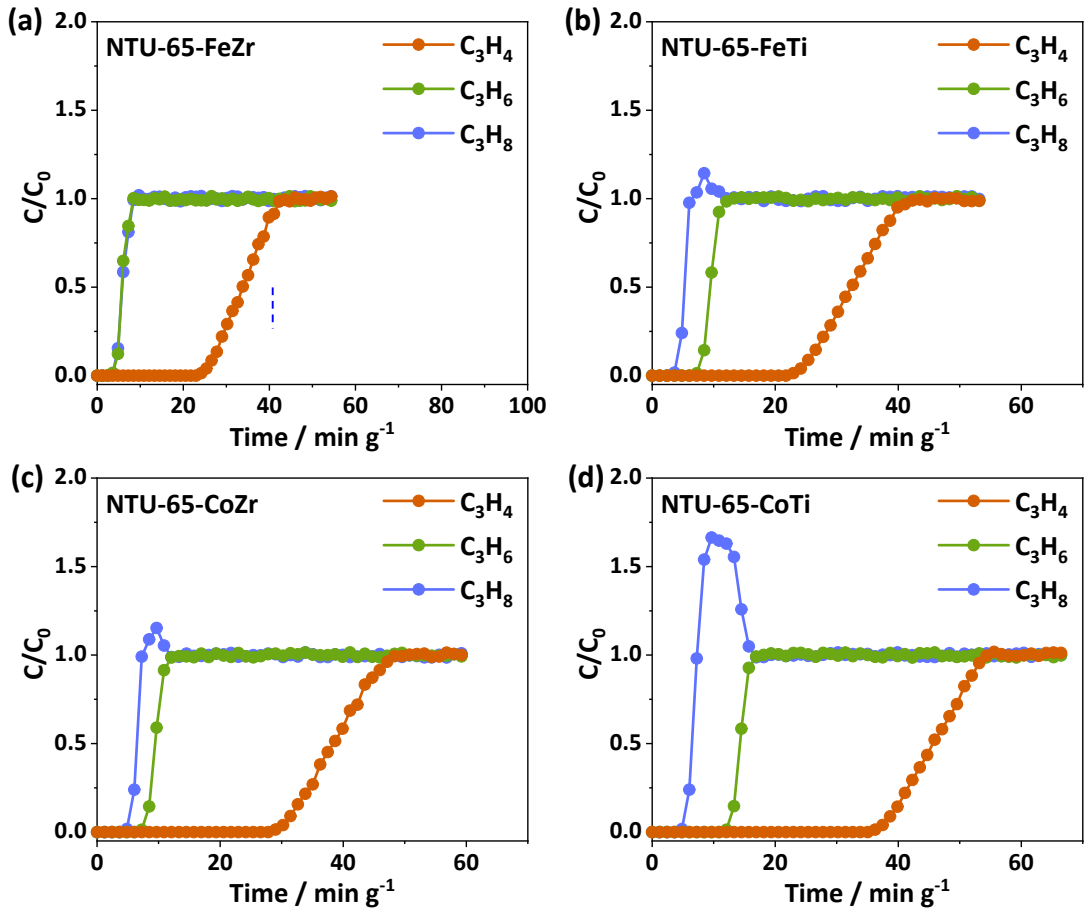

Figure S26. Experimental breakthrough curves of **NTU-65-FeZr** (a), **NTU-65-FeTi** (b), **NTU-65-CoZr** (c) and **NTU-65-CoTi** (d) for $C_3H_4/C_3H_6/C_3H_8$ (0.5/49.75/49.75, v/v/v) separation at 273 K (gas velocity: 10.0 mL·min^{-1}).

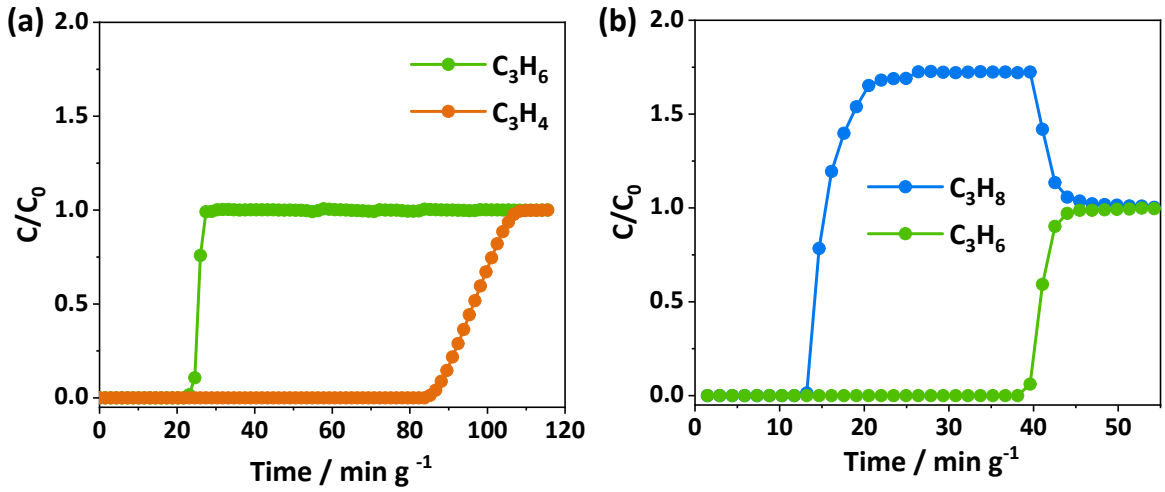

Figure S27. Experimental breakthrough curves of **NTU-65-CoTi**: (a) C_3H_4/C_3H_6 (1/99, v/v) and (a) C_3H_6/C_3H_8 (1/1, v/v) separation at 273 K (gas velocity: 2.0 mL/min).

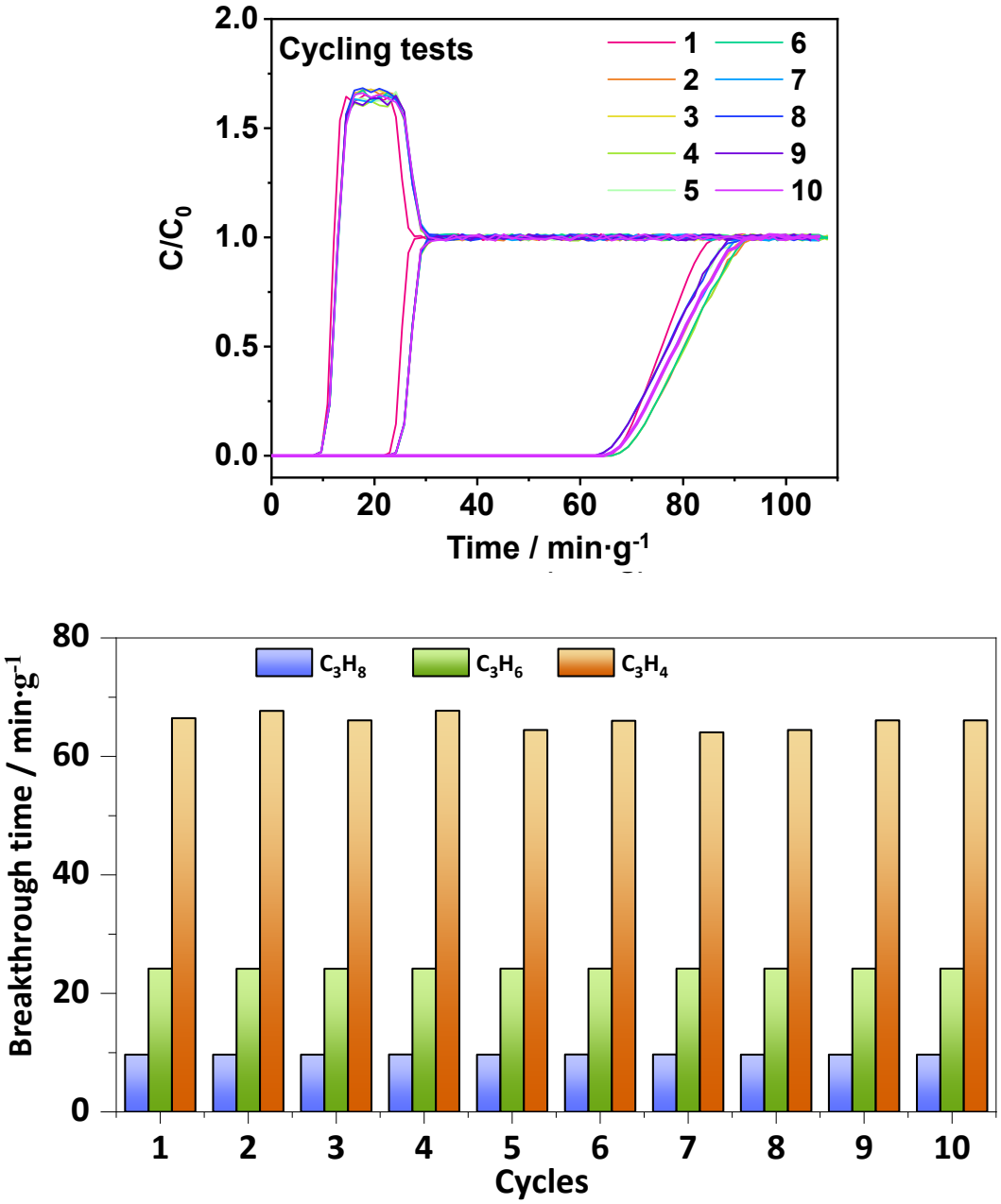

Figure S28. Cycling tests of **NTU-65-CoTi** for the $C_3H_4/C_3H_6/C_3H_8$ mixtures (0.5/49.75/49.75, v/v/v, 5.0 mL/min).

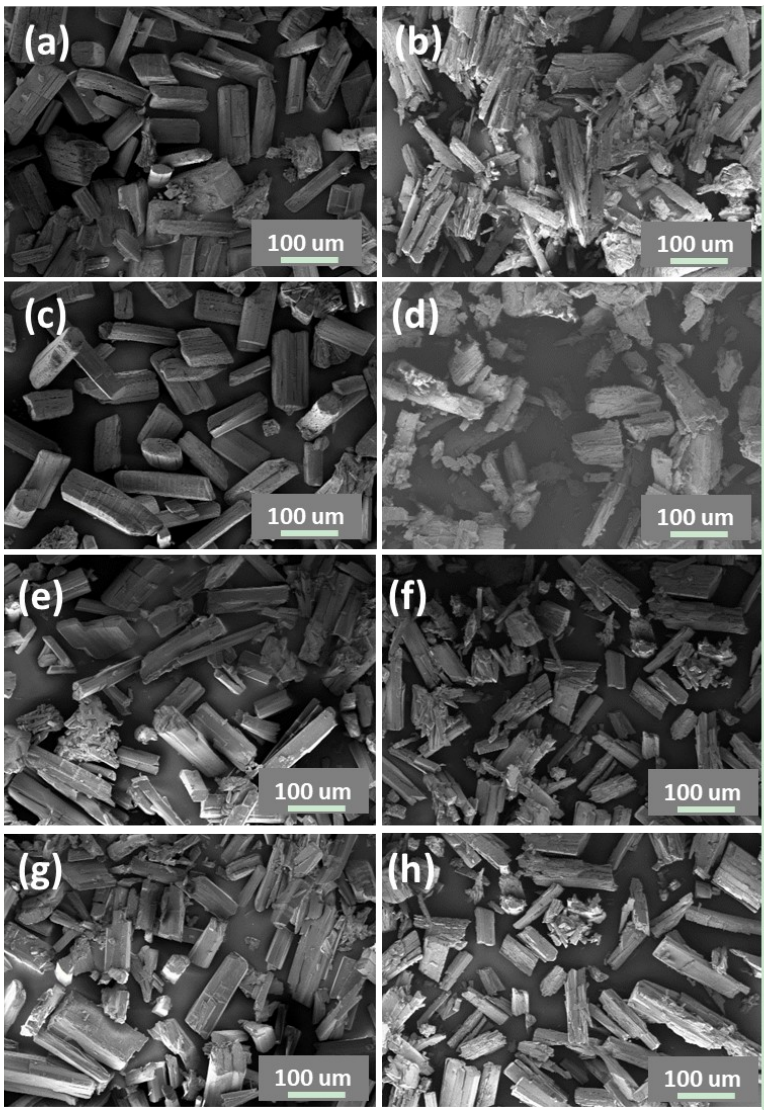

Figure S29. SEM patterns of **NTU-65-FeZr** (a, b), **NTU-65-FeTi** (c, d), **NTU-65-CoZr** (e, f) and **NTU-65-CoTi** (g, h) before activation and after breakthrough measurements.

Table S3. Uptakes ($mL \cdot g^{-1}$) of C_3H_4, C_3H_6 and C_3H_8 in **NTU-65-series** and other benchmark MOFs.

Compounds	Temp. (K)	C_3H_4 uptake		C_3H_6 uptake		C_3H_8 uptake		Uptake ratio of C_3H_4/C_3H_6 (0.1:0.5)	Uptake ratio of C_3H_6/C_3H_8 (0.5:0.5)	Uptake ratio of C_3H_4/C_3H_8 (0.1:0.5)	Ref.
		0.1 bar	1 bar	0.5 bar	1 bar	0.5 bar	1 bar				
Ternary separation											
NTU-65-CoTi	273	73.9	95.9	57.4	75.0	1.6	34.6	1.3	35.9	46.2	**This work**
NTU-65-CoZr		46.2	87.0	8.6	66.2	1.0	40.4	5.4	8.6	46.2	
NTU-65-FeTi		3.9	69.0	1.3	44.2	0.7	1.4	3.0	1.9	5.6	
NTU-65-FeZr		0.6	74.7	0.7	4.4	0.5	1.0	0.9	1.4	1.2	
C_3H_4/C_3H_6 separation											
UTSA-200	298	73.9	80.2	15.7	26.9	-	-	4.7	-	-	23
ZU-13	298	69.4	86.9	27.2	31.4	-	-	2.6	-	-	24
ELM-12	298	56.9	62.0	26.0	32.0	-	-	2.2	-	-	25
NbOFFIVE-1-Ni	298	38.5	42.3	21.3	27.5	-	-	1.8	-	-	26
SIFSIX-1-Cu		153.4	196.2	121.2	132.2	-	-	1.3	-	-	
SIFSIX-2-Cu-i		65.0	92.5	53.7	59.6	-	-	1.2	-	-	
SIFSIX-3-Zn		47.3	50.6	37.9	42.2	-	-	1.2	-	-	
SIFSIX-3-Ni		61.2	64.6	55.0	61.5	-	-	1.1	-	-	
NKMOF-1-Ni	298	53.8	78.4	38.4	46.0	-	-	1.4	-	-	27
ZU-62	298	67.4	83.0	53.0	60.6	-	-	1.3	-	-	28
Fe-MOF-74	318	149.4	177.9	136.6	148.5	-	-	1.1	-	-	29
SIFSIX-Cu-TPA	298	152.6	188.3	120.8	130.1	-	-	1.3	-	-	30
sql-NbOFFIVE-bpe-Cu-AB	298	53.7	65.1	42.4	47.0	-	-	1.3	-	-	31
GeFSIX-dps-Cu	273	74.6	86.7	1.8	1.8	-	-	41.4	-	-	32
GeFSIX-dps-Zn		49.7	85.1	1.8	1.8	-	-	27.6	-	-	
C_3H_6/C_3H_8 separation											
NTU-85	298	-	-	9.0	10.2	0.02	0.06	-	450	-	33
JUN-3a	273	-	-	65.6	69.4	56.3	58.7	-	1.2	-	34
	303	-	-	51.3	58.6	14.6	48.0	-	3.5	-	
HOF-16a	273	-	-	62.7	68.5	36.9	41.8	-	1.7	-	35
$Ni(BDC)(TED)_{0.5}$	273	-	-	152.3	160.9	144.7	151.8	-	1.1	-	36
Co-gallate	273	-	-	85.8	96.9	6.6	9.8	-	13.0	-	37
	298	-	-	30.1	40.1	2.8	3.1	-	10.8	-	
CPL-1	273			28.9	40.8	5.1	6.5	-	5.7	-	38
UTSA-400	298	-	-	38.1	42.3	1.1	1.1	-	34.6	-	39
NKU-FlexMOF-1	273	-	-	72.2	73.6	59.5	61.1	-	1.2	-	40
	298	-	-	69.6	69.9	63.5	65.7	-	1.1	-	
KAUST-7	298	-	-	25.2	31.4	0.5	2.0	-	50.4	-	41
Co_2(m-dobdc)	298			166.2	170.7	129.5	137.3	-	1.3	-	42
Y-abtc	298	-	-	43.0	44.3	1.4	1.4	-	30.7	-	43
Ni-NP	298	-	-	72.1	79.6	41.2	47.7	-	1.8	-	44
ZJU-75a	296	-	-	64.3	74.1	45.8	52.2	-	1.4	-	45

Note: "-"means no available data.

Table S4. Dual-site Langmuir-Freundlich fits for C_3H_4, C_3H_6 and C_3H_8 in **NTU-65-FeZr**.

	Site A				Site B			
	$\frac{q_{A,sat}}{\text{mol kg}^{-1}}$	$\frac{b_{A,0}}{\text{Pa}^{-\nu_A}}$	$\frac{E_A}{\text{kJ mol}^{-1}}$	ν_A	$\frac{q_{B,sat}}{\text{mol kg}^{-1}}$	$\frac{b_{B,0}}{\text{Pa}^{-\nu_B}}$	$\frac{E_B}{\text{kJ mol}^{-1}}$	ν_B
C_3H_4	3	9.503E-07	6.8	0.67	2.9	2.672E-105	343	8.85
C_3H_6	1	2.225E-51	38.7	8.35	4	2.793E-07	5.1	0.75
C_3H_6	0.4	1.104E-11	8.6	1.6	0.025	3.449E-11	35	0.85

Table S5. Dual-site Langmuir-Freundlich fits for C_3H_4, C_3H_6 and C_3H_8 in **NTU-65-FeTi**.

	Site A				Site B			
	$\frac{q_{A.sat}}{\text{mol kg}^{-1}}$	$\frac{b_{A,0}}{\text{Pa}^{-\nu_A}}$	$\frac{E_A}{\text{kJ mol}^{-1}}$	ν_A	$\frac{q_{B.sat}}{\text{mol kg}^{-1}}$	$\frac{b_{B,0}}{\text{Pa}^{-\nu_B}}$	$\frac{E_B}{\text{kJ mol}^{-1}}$	ν_B
C_3H_4	3	8.557E-15	45	1	2.35	2.693E-103	345	8.8
C_3H_6	2.05	4.991E-135	387	12.3	0.07	1.215E-06	11.5	0.8
C_3H_6	0.7	4.388E-22	65	1.5	0.85	4.621E-08	15	0.62

Table S6. Dual-site Langmuir-Freundlich fits for C_3H_4, C_3H_6 and C_3H_8 in **NTU-65-CoZr**.

	Site A				Site B			
	$\frac{q_{A.sat}}{\text{mol kg}^{-1}}$	$\frac{b_{A,0}}{\text{Pa}^{-\nu_A}}$	$\frac{E_A}{\text{kJ mol}^{-1}}$	ν_A	$\frac{q_{B.sat}}{\text{mol kg}^{-1}}$	$\frac{b_{B,0}}{\text{Pa}^{-\nu_B}}$	$\frac{E_B}{\text{kJ mol}^{-1}}$	ν_B
C_3H_4	1.4	3.538E-20	65	1.6	2.6	3.147E-76	259	6.6
C_3H_6	2.8	3.406E-109	302	10.6	2.6	2.832E-07	11.7	0.56
C_3H_6	2.6	9.609E-85	216	8.6	1	6.420E-07	10	0.6

Table S7. Dual-site Langmuir-Freundlich fits for C_3H_4, C_3H_6 and C_3H_8 in **NTU-65-CoTi**.

	Site A				Site B			
	$\frac{q_{A,sat}}{\text{mol kg}^{-1}}$	$\frac{b_{A,0}}{\text{Pa}^{-\nu_A}}$	$\frac{E_A}{\text{kJ mol}^{-1}}$	ν_A	$\frac{q_{B,sat}}{\text{mol kg}^{-1}}$	$\frac{b_{B,0}}{\text{Pa}^{-\nu_B}}$	$\frac{E_B}{\text{kJ mol}^{-1}}$	ν_B
C_3H_4	1.6	4.130E-18	59	1.45	2.8	1.321E-70	250	6.1
C_3H_6	3.2	3.359E-66	225	4.9	2.9	3.229E-05	2	0.51
C_3H_6	2.1	2.844E-56	120	6.6	0.02	3.360E-07	9.7	1.2

Notation

b	Langmuir-Freundlich constant, $\text{Pa}^{-\nu}$
E	energy parameter, J mol^{-1}
L	length of packed bed adsorber, m
m_{ads}	mass of adsorbent packed in fixed bed, kg
q	component molar loading of species *i*, mol kg^{-1}
q_{sat}	saturation loading, mol kg^{-1}
Q_0	volumetric flow rate of gas mixture entering fixed bed, m^3 s^{-1}
Q_{st}	isosteric heat of adsorption, J mol^{-1}
T	absolute temperature, K

Greek letters

v	Freundlich exponent, dimensionless

Reference

1. G. M. Sheldrick, A short history of SHELX, *Acta Crystallogr. Sec. A*, 2008, **64**, 112-122.
2. A. L. Spek, *PLATON, A Multipurpose Crystallographic Tool (Utrecht University,2001).*
3. P. Vandersluis and A. L. Spek, Bypass - an Effective Method for the Refinement of Crystal-Structures Containing Disordered Solvent Regions, *Acta Crystallogr. Sec. A*, 1990, **46**, 194-201.
4. R. Krishna, The Maxwell-Stefan description of mixture diffusion in nanoporous crystalline materials, *Microporous Mesoporous Mater.*, 2014, **185**, 30-50.
5. R. Krishna, Methodologies for Evaluation of Metal-Organic Frameworks in Separation Applications, *RSC Advances*, 2015, **5**, 52269-52295.
6. R. Krishna, Screening Metal-Organic Frameworks for Mixture Separations in Fixed-Bed Adsorbers using a Combined Selectivity/Capacity Metric, *RSC Advances*, 2017, **7**, 35724-35737.
7. R. Krishna, Methodologies for Screening and Selection of Crystalline Microporous Materials in Mixture Separations, *Sep. Purif. Technol.*, 2018, **194**, 281-300.
8. R. Krishna, Metrics for Evaluation and Screening of Metal-Organic Frameworks for Applications in Mixture Separations, *ACS Omega*, 2020, **5**, 16987−17004.
9. D. Frenkel and B. Smit, Understanding Molecular Simulation: From Algorithms to Applications, *Academic Press, San Diego*, 2002.
10. D. Dubbeldam, S. Calero, D. E. Ellis and R. Q. Snurr, RASPA: molecular simulation software for adsorption and diffusion in flexible nanoporous materials, *Mol. Simul.*, 2016, **42**, 81-101.
11. A. K. Rappe, C. J. Casewit, K. S. Colwell, W. A. Goddard and W. M. Skiff, Uff, a Full Periodic-Table Force-Field for Molecular Mechanics and Molecular-Dynamics Simulations, *J. Am. Chem. Soc.*, 1992, **114**, 10024-10035.
12. T. A. Manz and N. G. Limas, Introducing DDEC6 atomic population analysis: part 1. Charge partitioning theory and methodology, *Rsc Adv*, 2016, **6**, 47771-47801.
13. Y.-L. Peng, C. He, T. Pham, T. Wang, P. Li, R. Krishna, K. A. Forrest, A. Hogan, S. Suepaul, B. Space, M. Fang, Y. Chen, M. J. Zaworotko, J. Li, L. Li, Z. Zhang, P. Cheng and B. Chen, Robust Microporous Metal–Organic Frameworks for Highly Efficient and Simultaneous Removal of Propyne and Propadiene from Propylene, *Angew. Chem. Int. Ed.*, 2019, **58**, 10209-10214.
14. J. P. Perdew, K. Burke and M. Ernzerhof, Generalized gradient approximation made simple, *Phys. Rev. Lett.*, 1996, **77**, 3865-3868.
15. S. Grimme, J. Antony, S. Ehrlich and H. Krieg, A consistent and accurate ab initio parametrization of density functional dispersion correction (DFT-D) for the 94 elements H-Pu, *J. Chem. Phys.*, 2010, **132**, 154104-154122.
16. G. Kresse and J. Furthmuller, Efficiency of ab-initio total energy calculations for metals and semiconductors using a plane-wave basis set, *Comp. Mater. Sci.*, 1996, **6**, 15-50.
17. G. Kresse and J. Furthmuller, Efficient iterative schemes for ab initio total-energy calculations using a plane-wave basis set, *Phys. Rev. B*, 1996, **54**, 11169-11186.
18. P. E. Blochl, Projector Augmented-Wave Method, *Phys. Rev. B*, 1994, **50**, 17953-17979.
19. G. Kresse and D. Joubert, From ultrasoft pseudopotentials to the projector augmented-wave method, *Phys. Rev. B*, 1999, **59**, 1758-1775.
20. S. L. Dudarev, G. A. Botton, S. Y. Savrasov, C. J. Humphreys and A. P. Sutton, Electron-energy-loss spectra and the structural stability of nickel oxide: An LSDA+U study, *Phys. Rev. B*, 1998, **57**, 1505-1509.
21. L. Wang, T. Maxisch and G. Ceder, Oxidation energies of transition metal oxides within the GGA+U framework, *Phys. Rev. B*, 2006, **73**, 195107-195112.
22. V. Stevanovi, S. Lany, X. Zhang and A. Zunger, Correcting density functional theory for accurate predictions of

compound enthalpies of formation: Fitted elemental-phase reference energies, *Phys. Rev. B*, 2012, 115104-115115.

23. L. B. Li, H. M. Wen, C. H. He, R. B. Lin, R. Krishna, H. Wu, W. Zhou, J. P. Li, B. Li and B. L. Chen, A Metal-Organic Framework with Suitable Pore Size and Specific Functional Sites for the Removal of Trace Propyne from Propylene, *Angew. Chem. Int. Ed.*, 2018, **57**, 15183-15188.
24. L. F. Yang, X. L. Cui, Y. B. Zhang, Q. W. Yang and H. B. Xing, A highly sensitive flexible metal-organic framework sets a new benchmark for separating propyne from propylene, *J. Mater. Chem. A*, 2018, **6**, 24452-24458.
25. L. B. Li, R. B. Lin, R. Krishna, X. Q. Wang, B. Li, H. Wu, J. P. Li, W. Zhou and B. L. Chen, Flexible-Robust Metal-Organic Framework for Efficient Removal of Propyne from Propylene, *J. Am. Chem. Soc.*, 2017, **139**, 7733-7736.
26. L. F. Yang, X. L. Cui, Q. W. Yang, S. H. Qian, H. Wu, Z. B. Bao, Z. G. Zhang, Q. L. Ren, W. Zhou, B. L. Chen and H. B. Xing, A Single-Molecule Propyne Trap: Highly Efficient Removal of Propyne from Propylene with Anion-Pillared Ultramicroporous Materials, *Adv. Mater.*, 2018, **30**, 1705374-1705381.
27. Y. L. Peng, C. H. He, T. Pham, T. Wang, P. F. Li, R. Krishna, K. A. Forrest, A. Hogan, S. Suepaul, B. Space, M. Fang, Y. Chen, M. J. Zaworotko, J. P. Li, L. B. Li, Z. J. Zhang, P. Cheng and B. L. Chen, Robust Microporous Metal-Organic Frameworks for Highly Efficient and Simultaneous Removal of Propyne and Propadiene from Propylene, *Angew. Chem. Int. Ed.*, 2019, **58**, 10209-10214.
28. L. F. Yang, X. L. Cui, Z. Q. Zhang, Q. W. Yang, Z. B. Bao, Q. L. Ren and H. B. Xing, An Asymmetric Anion-Pillared Metal-Organic Framework as a Multisite Adsorbent Enables Simultaneous Removal of Propyne and Propadiene from Propylene, *Angew. Chem. Int. Ed.*, 2018, **57**, 13145-13149.
29. E. D. Bloch, W. L. Queen, R. Krishna, J. M. Zadrozny, C. M. Brown and J. R. Long, Hydrocarbon Separations in a Metal-Organic Framework with Open Iron(II) Coordination Sites, *Science*, 2012, **335**, 1606-1610.
30. Y. J. Jiang, L. Y. Wang, T. A. Yan, J. B. Hu, W. Q. Sun, R. Krishna, D. M. Wang, Z. L. Gu, D. H. Liu, X. L. Cui, H. B. Xing and Y. B. Zhang, Insights into the thermodynamic-kinetic synergistic separation of propyne/propylene in anion pillared cage MOFs with entropy-enthalpy balanced adsorption sites, *Chem. Sci.*, 2023, **14**, 298-309.
31. M.-Y. Gao, A. A. Bezrukov, B.-Q. Song, M. He, S. J. Nikkhah, S.-Q. Wang, N. Kumar, S. Darwish, D. Sensharma, C. Deng, J. Li, L. Liu, R. Krishna, M. Vandichel, S. Yang and M. J. Zaworotko, Highly Productive C_3H_4/C_3H_6 Trace Separation by a Packing Polymorph of a Layered Hybrid Ultramicroporous Material, *J. Am. Chem. Soc.*, 2023, **145**, 11837-11845.
32. T. Ke, Q. Wang, J. Shen, J. Zhou, Z. Bao, Q. Yang and Q. Ren, Molecular Sieving of C-2-C-3 Alkene from Alkyne with Tuned Threshold Pressure in Robust Layered Metal-Organic Frameworks, *Angew. Chem. Int. Ed.*, 2020, **59**, 12725-12730.
33. Q. Dong, Y. Huang, J. Wan, Z. Lu, Z. Wang, C. Gu, J. Duan and J. Bai, Confining Water Nanotubes in a $Cu_{10}O_{13}$-Based Metal–Organic Framework for Propylene/Propane Separation with Record-High Selectivity, *J. Am. Chem. Soc.*, 2023, **145**, 8043-8051.
34. H. Zeng, M. Xie, T. Wang, R.-J. Wei, X.-J. Xie, Y. Zhao, W. Lu and D. Li, Orthogonal-array dynamic molecular sieving of propylene/propane mixtures, *Nature*, 2021, **595**, 542-548.
35. J. Gao, Y. Cai, X. Qian, P. Liu, H. Wu, W. Zhou, D.-X. Liu, L. Li, R.-B. Lin and B. Chen, A Microporous Hydrogen-Bonded Organic Framework for the Efficient Capture and Purification of Propylene, *Angew. Chem. Int. Ed.*, 2021, **60**, 20400-20406.
36. M. Chang, J. Ren, Y. Wei, J.-X. Wang, Q. Yang, D. Liu and J.-F. Chen, A robust metal-organic framework with guest molecules induced splint-like pore confinement to construct propane-trap for propylene purification, *Sep. Purif. Technol.*, 2021, **279**, 119656.
37. B. Liang, X. Zhang, Y. Xie, R. B. Lin, R. Krishna, H. Cui, Z. Q. Li, Y. S. Shi, H. Wu, W. Zhou and B. L. Chen, An Ultramicroporous Metal-Organic Framework for High Sieving Separation of Propylene from Propane, *J. Am. Chem. Soc.*, 2020, **142**, 17795-17801.
38. Y. Chen, Z. Qiao, D. Lv, C. Duan, X. Sun, H. Wu, R. Shi, Q. Xia and Z. Li, Efficient adsorptive separation of C_3H_6 over

C_3H_8 on flexible and thermoresponsive CPL-1, *Chem. Eng. J.*, 2017, **328**, 360-367.

39. Y. Xie, Y. S. Shi, E. M. C. Morales, A. El Karch, B. Wang, H. Arman, K. Tan and B. L. Chen, Optimal Binding Affinity for Sieving Separation of Propylene from Propane in an Oxyfluoride Anion-Based Metal-Organic Framework, *J. Am. Chem. Soc.*, 2023, **145**, 2386-2394.
40. M.-H. Yu, B. Space, D. Franz, W. Zhou, C. He, L. Li, R. Krishna, Z. Chang, W. Li, T.-L. Hu and X.-H. Bu, Enhanced Gas Uptake in a Microporous Metal–Organic Framework via a Sorbate Induced-Fit Mechanism, *J. Am. Chem. Soc.*, 2019, **141**, 17703-17712.
41. A. Cadiau, K. Adil, P. M. Bhatt, Y. Belmabkhout and M. Eddaoudi, A metal-organic framework-based splitter for separating propylene from propane, *Science*, 2016, **353**, 137-140.
42. J. E. Bachman, M. T. Kapelewski, D. A. Reed, M. I. Gonzalez and J. R. Long, M_2(m-dobdc) (M = Mn, Fe, Co, Ni) Metal-Organic Frameworks as Highly Selective, High-Capacity Adsorbents for Olefin/Paraffin Separations, *J. Am. Chem. Soc.*, 2017, **139**, 15363-15370.
43. H. Wang, X. Dong, V. Colombo, Q. Wang, Y. Liu, W. Liu, X.-L. Wang, X.-Y. Huang, D. M. Proserpio, A. Sironi, Y. Han and J. Li, Tailor-Made Microporous Metal-Organic Frameworks for the Full Separation of Propane from Propylene Through Selective Size Exclusion, *Adv. Mater.*, 2018, **30**, 1805088.
44. Y. Xie, Y. Shi, H. Cui, R.-B. Lin and B. Chen, Efficient Separation of Propylene from Propane in an Ultramicroporous Cyanide-Based Compound with Open Metal Sites, *Small Struct.*, 2021, **3**, 2100125.
45. D. Liu, J. Y. Pei, X. Zhang, X. W. Gu, H. M. Wen, B. L. Chen, G. D. Qian and B. Li, Scalable Green Synthesis of Robust Ultra-Microporous Hofmann Clathrate Material with Record C_3H_6 Storage Density for Efficient C_3H_6/C_3H_8 Separation, *Angew. Chem. Int. Ed.*, 2023, **62**, e202218590.